

SR-LIO: LiDAR-Inertial Odometry with Sweep Reconstruction

Zikang Yuan¹, Fengtian Lang² and Xin Yang^{2*}

Abstract—This paper proposes a novel LiDAR-inertial odometry (LIO), named SR-LIO, based on an improved bundle adjustment (BA) framework. The core of our SR-LIO is a novel sweep reconstruction method, which segments and reconstructs raw input sweeps from spinning LiDAR to obtain reconstructed sweeps with higher frequency. Such method can effectively reduce the time interval for each IMU pre-integration, reducing the IMU pre-integration error and enabling the usage of BA based LIO optimization. In order to make all the states during the period of a reconstructed sweep can be equally optimized, we further propose multi-segment joint LIO optimization, which allows the state of each sweep segment to be constrained from both LiDAR and IMU. Experimental results on three public datasets demonstrate that our SR-LIO outperforms all existing state-of-the-art methods on accuracy, and reducing the IMU pre-integration error via the proposed sweep reconstruction is very importance for the success of a BA based LIO framework. The source code of SR-LIO is publicly available for the development of the community.

Index Terms—SLAM, Sensor Fusion, Localization, Mapping.

I. INTRODUCTION

THREE-dimension light detection and ranging (LiDAR) can directly capture accurate and dense scene structure information in a large range and thus has become one of the mainstream sensors in outdoor robots and autonomous driving fields. An odometry utilizing only 3D LiDAR [1]–[7] has the ability to estimate accurate pose in most scenarios, and transform the point clouds collected at different times to a unified coordinate system. However, there are still the two main problems in LiDAR-only odometry: 1) Most, if not all, existing LiDAR odometry rely on the Iterative Closest Point (ICP) algorithm [8]–[10] for pose estimation while the accuracy of ICP largely depends on the initial motion value which could be unreliable and in turn yield inaccurate pose estimation. 2) For scenes without rich geometric structure information, the commonly used point-to-plane ICP algorithm usually fails due to lack of sufficiently reliable constraints for pose estimation. Introducing Inertial Measurement Unit (IMU) as an additional sensor is a promising solution to address the above two problems with little memory and time consumption.

Existing LiDAR-inertial odometry (LIO) systems [1]–[3], [11]–[17] can be divided into two groups: loosely-coupled and

tightly-coupled. The loose-coupled framework [1]–[3] mainly uses IMU measurements to calibrate the motion distortion of LiDAR point clouds, and provide motion priors for ICP pose estimation. On the basis of loose-coupling, the tight-coupled framework [11]–[17] also uses IMU measurements to provide motion constraints for ICP, so as to achieve more accurate and robust state estimation. The LIO joint optimization systems based on the tightly-coupled framework can be mainly categorized into three types: iterated extended Kalman filter (iEKF) [13], [15], [16], bundle adjustment (BA) [11], [12] and graph optimization [14], [17]. The performance of all these three types both depends on the precision of IMU pre-integration [18]. Specifically, pre-integration is a state variable obtained by integrating IMU measurements over the period of a full sweep, which is used to provide motion constraints during LIO joint optimization. As inevitable errors exist in IMU measurements, a long integration time will lead to a large cumulative error of pre-integration. In general, the time interval between two consecutive sweeps is 100ms, which makes IMU pre-integration has a large and non-reducible accumulative error. If some key-sweeps are selected in a series of consecutive sweeps, the time interval between two key-sweeps is even longer, further increasing the accumulative error in pre-integration.

In this paper, we propose sweep reconstruction, which segments and reconstructs raw input sweeps from spinning LiDAR to obtain reconstructed sweeps with higher frequency. Specifically, the sweep reconstruction method uses the characteristics of continuous scanning of spinning LiDAR to segment each full sweep into 3 sweep segments, and then successively join each sweep segment together with the next 2 sweep segments to obtain a reconstructed full sweep (as shown in Fig. 1). After performing the above steps for each sweep segment, each raw sweep becomes 3 reconstructed full sweeps, whose frequency are 3X higher. The increased frequency shortens the time interval between two consecutive sweeps, and thus reduces the error of IMU pre-integration. Therefore, sweep reconstruction can not only increase the frequency of sweeps, but also improve the accuracy of LIO joint optimization via reducing IMU pre-integration errors.

It has been identified in our previous study that, BA based framework is very sensitive to the IMU pre-integration error. To address this issue, we integrate the proposed sweep reconstruction method into our BA-based LIO system to derived our SR-LIO. The proposed SR-LIO firstly down-samples the 10 Hz input sweeps, and then performs sweep reconstruction to obtain the 30 Hz reconstructed sweeps. Next, for each reconstructed sweep we perform LIO joint state optimization,

This work was not supported by any organization.

¹Zikang Yuan is with Institute of Artificial Intelligence, Huazhong University of Science and Technology, Wuhan, 430074, China. (E-mail: yzk2020@hust.edu.cn)

²Fengtian Lang and Xin Yang are with the Electronic Information and Communications, Huazhong University of Science and Technology, Wuhan, 430074, China. (* represents the corresponding author. E-mail: U201913666@hust.edu.cn; xinyang2014@hust.edu.cn)

in which the IMU pre-integration period is 33ms due to sweep reconstruction, but the reconstructed sweep maintains a full sweep which lasts 100ms (shown in Fig. 1). In order to better maintain trajectory consistency, we propose a novel multi-segment joint optimization approach, which fully utilizes both IMU constraints and state variables located in each 100ms period for optimization. After the state of a current reconstructed sweep is optimized, we add the point clouds of the current reconstructed sweep to the map. Since there are duplicate points in the consecutive reconstructed sweeps, we perform map update at the same frequency as raw input sweeps (10Hz) to prevent the same point cloud from being added repeatedly.

To summarize, the main contributions of this work are three folds: 1) We propose a sweep reconstruction method, which can increase the frequency of spinning LiDAR sweeps and reduce the error of IMU pre-integration in LIO systems; 2) We embed the proposed sweep reconstruction method into our newly designed BA based LIO system and achieve the state-of-the-art accuracy; 3) We have released the source code of this work for the development of the community¹.

The rest of this paper is structured as follows. In Sec. II, we briefly discuss the relevant literature. Sec. III provides preliminaries. Then Secs. IV and V presents details of the proposed sweep reconstruction method and our system SR-LIO. Sec. VI provides experimental evaluation. In Sec. VII, we conclude the paper.

II. RELATED WORK

LiDAR-Only Odometry. LiDAR-based odometry systems [1]–[7] rely on geometric information contained in LiDAR point clouds for tracking, and constantly register the new point cloud to the map. LOAM [1], [2] is the most classical LiDAR odometry, which mainly consists of three steps: 1) Extracting edge and surface features from raw point clouds; 2) Performing sweep-to-sweep pose estimation; 3) Performing sweep-to-map pose optimization and utilizing the optimized pose to register point clouds to the map. However, due to huge number of 3D point clouds to be processed, the output frequency of LOAM is low. On the basis of LOAM, LeGO-LOAM [3] proposes to group raw point clouds into several clusters, and removes clusters with weak geometric structure information to reduce computation. However, accurately removing clusters with weak geometry is a nontrivial task, and incorrect removal of useful clusters would degrade the accuracy and robustness of pose estimation. SuMa [7] proposes to represent the map via a surfel-based representation that aggregates information from point clouds. However, GPU acceleration is necessary for SuMa to achieve real-time performance, and the pose estimation accuracy of SuMa is not better than systems based on the framework of LOAM. Fast-LOAM eliminates the sweep-to-map pose optimization module and only retains the sweep-to-sweep pose estimation module. This operation greatly reduces the computational burden, however, the accuracy of pose estimation is sacrificed. In [4], authors propose intensity scan context (ISC) to improve the performance of loop detection

based on Fast-LOAM. IMLS-LOAM [5] proposes an IMLS pose solution algorithm to replace conventional transport ICP. However, large computational cost of IMLS makes IMLS-LOAM impossible to run in real time. On the basis of IMLS-LOAM, CT-ICP [6] proposes that it is necessary to estimate the state of two moments in each sweep: 1) at the beginning time of the sweep, and 2) at the end time of the sweep. By this way, the state at any time during this sweep can be expressed as a function of the state at the beginning time and the state at the end time. Compared with the previous scheme [1]–[5], [7] of representing the state of a sweep by the state only at beginning time or end time, CT-ICP is more realistic and meanwhile achieves superior performance.

LiDAR-Inertial Odometry. LiDAR-inertial odometry systems [1]–[3], [11]–[17] are mainly divided into loosely-coupled framework [1]–[3] and tightly-coupled framework [11]–[17]. The loose-coupled framework, e.g., LOAM [1], [2] and LeGO-LOAM [3] which have an IMU interface, uses IMU measurements to calibrate the motion distortion of LiDAR point clouds, and provides motion priors for ICP pose estimation. The tightly-coupled framework [11]–[17] uses IMU measurements to provide motion constraints for ICP, so as to improve pose estimation accuracy and robustness. According to the type of LIO joint optimization, the tightly-coupled system can be further divided into iEKF based framework [13], [15], [16], BA based framework [11], [12] and graph optimization based framework [14], [17]. LINs firstly fuses 6-axis IMU and 3D LiDAR in an iEKF based framework, where an iEKF is designed to correct the estimated state recursively by generating new feature correspondences in each iteration, and to keep the system computationally tractable. Based on the mathematical derivation, Fast-LIO [15] proposes a new method of solving Kalman gain to avoid the calculation of the high-order matrix inversion, and in turn greatly reduce the computational burden. Based on Fast-LIO, Fast-LIO2 [16] proposes an ikd-tree algorithm [19]. Compared with the original kd-tree, ikd-tree reduces time cost in building a tree, traversing a tree, removing elements and other operations. LIO-SAM [14] firstly formulates LIO odometry as a factor graph. Such formulation allows a multitude of relative and absolute measurements, including loop closures, to be incorporated from different sources as factors into the system. DLIO [17] builds an internal map by registering dense point clouds to a local submap with a translational and rotational prior generated by a nonlinear motion model. [12] firstly fuses 6-axis IMU and 3D LiDAR in a BA based framework. Besides, to obtain more reliable poses estimation, a rotation-constrained refinement algorithm is proposed to further align the pose with the global map. LiLi-OM [11] selects the key-sweeps from solid-state LiDAR data, and performs BA based multi-key-sweep joint LIO-optimization. However, when the type of LiDAR changes from solid-state to spinning, the time interval between two consecutive key-sweeps becomes longer than 100ms, then the error of IMU constraints in LiLi-OM is larger than that of [12]. In this case, the accumulative error in IMU pre-integration cannot be ignored no matter what kind of tightly-coupled framework is used. If the key-sweep selection is needed, e.g., [11], the time interval of two consecutive key-sweeps becomes

¹https://github.com/ZikangYuan/sr_lio

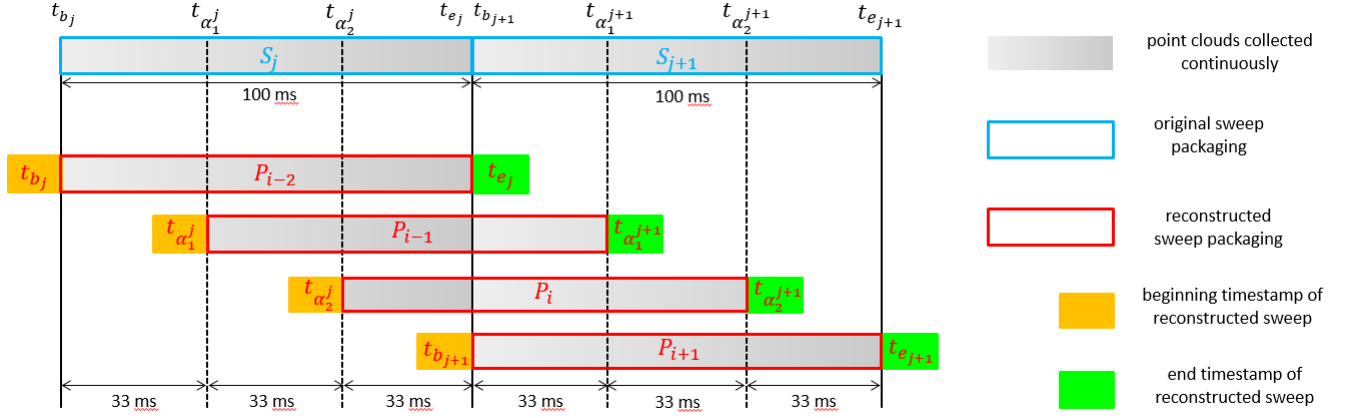


Fig. 1. Illustration of the proposed sweep reconstruction method, which splits the original sweep packet into continuous point cloud data streams, and then re-packages point cloud data streams in a multiplexing way to obtain sweeps with higher frequency.

even longer, further increasing the accumulative error in IMU pre-integration, and consequently reduce the accuracy and robustness of a system.

III. PRELIMINARY

A. Coordinate Systems

We denote $(\cdot)^w$, $(\cdot)^l$ and $(\cdot)^o$ as a 3D point in the world coordinates, the LiDAR coordinates and the IMU coordinates respectively. The world coordinates coincide with $(\cdot)^o$ at the starting position.

We denote the LiDAR coordinates for taking the i_{th} sweep at time t_i as l_i and the corresponding IMU coordinates at t_i as o_i , then the transformation matrix (i.e., external parameters) from l_i to o_i is denoted as $\mathbf{T}_{l_i}^{o_i} \in SE(3)$:

$$\mathbf{T}_{l_i}^{o_i} = \begin{bmatrix} \mathbf{R}_{l_i}^{o_i} & \mathbf{t}_{l_i}^{o_i} \\ \mathbf{0} & 1 \end{bmatrix} \quad (1)$$

where $\mathbf{T}_{l_i}^{o_i}$ consists of a rotation matrix $\mathbf{R}_{l_i}^{o_i} \in SO(3)$ and a translation vector $\mathbf{t}_{l_i}^{o_i} \in \mathbb{R}^3$. The external parameters are usually calibrated once offline and remain constant during online pose estimation. Therefore, we can represent $\mathbf{T}_{l_i}^{o_i}$ using \mathbf{T}_l^o for simplicity. In the following statement, we omit the index that represents the coordinate system for simplified notation. For instance, the pose from the IMU coordinates to the world coordinate is strictly defined as $\mathbf{T}_{o_i}^w$, yet represented as \mathbf{T}_i^w for simplicity.

In addition to pose, we also estimate the velocity \mathbf{v} , the accelerometer bias \mathbf{b}_a and the gyroscope bias \mathbf{b}_ω , which are represented uniformly by a state vector:

$$\mathbf{x} = [\mathbf{t}^T, \mathbf{q}^T, \mathbf{v}^T, \mathbf{b}_a^T, \mathbf{b}_\omega^T]^T \quad (2)$$

where \mathbf{q} is the quaternion form of the rotation matrix \mathbf{R} .

B. Sweep State Expression

Inspired by CT-ICP [6], we represent the state of a sweep S by: 1) the state at the beginning time t_b of S (e.g., \mathbf{x}_b) and 2) the state at the end time t_e of S (e.g., \mathbf{x}_e). By this way, the

state of each point cloud during $[t_b, t_e]$ can be represented as a function of \mathbf{x}_b and \mathbf{x}_e . For instance, for a point cloud $\mathbf{p} \in S$ collected at time $t_p \in [t_b, t_e]$, the state at t_p can be calculated as:

$$\begin{aligned} \alpha &= \frac{t_p - t_b}{t_e - t_b} \\ \mathbf{t}_p &= (1 - \alpha)\mathbf{t}_b + \alpha\mathbf{t}_e \\ \mathbf{q}_p &= \mathbf{q}_b \cdot \text{slerp}(\alpha, \mathbf{q}_e) \\ \mathbf{v}_p &= (1 - \alpha)\mathbf{v}_b + \alpha\mathbf{v}_e \\ \mathbf{b}_{a_p} &= (1 - \alpha)\mathbf{b}_{a_b} + \alpha\mathbf{b}_{a_e} \\ \mathbf{b}_{\omega_p} &= (1 - \alpha)\mathbf{b}_{\omega_b} + \alpha\mathbf{b}_{\omega_e} \end{aligned} \quad (3)$$

where $\text{slerp}(\cdot)$ is the spherical linear interpolation operator for quaternion.

C. IMU Measurement Model

An IMU consists of an accelerometer and a gyroscope. The raw gyroscope and accelerometer measurements from IMU, $\hat{\mathbf{a}}_t$ and $\hat{\boldsymbol{\omega}}_t$, are given by:

$$\begin{aligned} \hat{\mathbf{a}}_t &= \mathbf{a}_t + \mathbf{b}_{a_t} + \mathbf{R}_w^t \mathbf{g}^w + \mathbf{n}_a \\ \hat{\boldsymbol{\omega}}_t &= \boldsymbol{\omega}_t + \mathbf{b}_{\omega_t} + \mathbf{n}_\omega \end{aligned} \quad (4)$$

IMU measurements, which are measured in the IMU coordinates, combine the force for countering gravity and the platform dynamics, and are affected by acceleration bias \mathbf{b}_{a_t} , gyroscope bias \mathbf{b}_{ω_t} , and additive noise. As mentioned in VINs-Mono [20], the additive noise in acceleration and gyroscope measurements can be modeled as Gaussian white noise, $\mathbf{n}_a \sim N(\mathbf{0}, \sigma_a^2)$, $\mathbf{n}_\omega \sim N(\mathbf{0}, \sigma_\omega^2)$. Acceleration bias and gyroscope bias are modeled as random walk, whose derivatives are Gaussian, $\dot{\mathbf{b}}_{a_t} = \mathbf{n}_{b_a} \sim N(\mathbf{0}, \sigma_{b_a}^2)$, $\dot{\mathbf{b}}_{\omega_t} = \mathbf{n}_{b_\omega} \sim N(\mathbf{0}, \sigma_{b_\omega}^2)$.

IV. SWEEP RECONSTRUCTION

Sweep reconstruction aims to derive a 30 Hz reconstructed sweep P from the 10 Hz raw input LiDAR sweep S . Fig. 1 illustrates the core idea of our sweep reconstruction. Given the last sweep S_j which begins at t_{b_j} and ends at t_{e_j} , and the

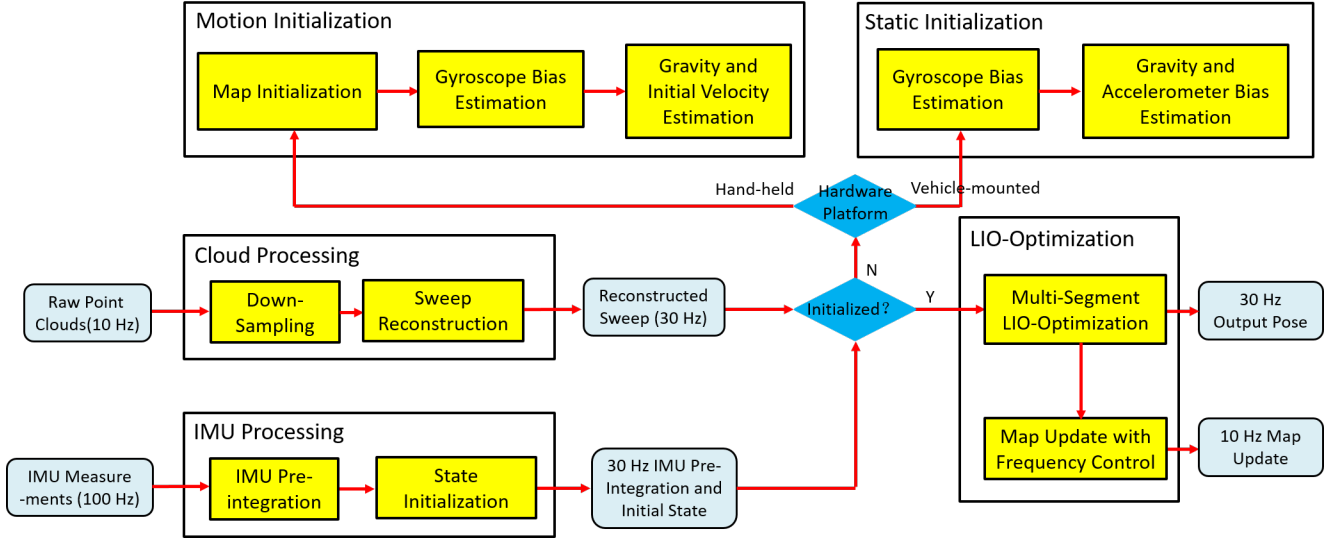


Fig. 2. Overview of our SR-LIO which consists of four main modules: a cloud processing module, an IMU processing module, an initialization module and a LIO-Optimization module.

current input sweep S_{j+1} which begins at $t_{b_{j+1}}$ and ends at $t_{e_{j+1}}$, we assume the lengths of time intervals $[t_{b_j}, t_{e_j}]$ and $[t_{b_{j+1}}, t_{e_{j+1}}]$ are both 100ms. Based on the characteristics of continuous acquisition over a period of time of LiDAR, we can split the original sweep packet into continuous point cloud data streams, and then re-package point cloud data streams in a multiplexing way to obtain sweeps with higher frequency. Specifically, we first calculate three equal points of the time interval $[t_{b_j}, t_{e_j}]$ and $[t_{b_{j+1}}, t_{e_{j+1}}]$ (e.g., $t_{\alpha_1^j}, t_{\alpha_2^j}, t_{\alpha_1^{j+1}}$ and $t_{\alpha_2^{j+1}}$), and put all time stamps in a set:

$$T = \{t_{b_j}, t_{\alpha_1^j}, t_{\alpha_2^j}, t_{e_j}, t_{b_{j+1}}, t_{\alpha_1^{j+1}}, t_{\alpha_2^{j+1}}, t_{e_{j+1}}\} \quad (5)$$

Then we take each element of T (i.e., $T[k]$) as the beginning time stamp and take $T[k+3]$ as the end time stamp. We re-package the point cloud data streams during $[T[k], T[k+3]]$ to obtain the reconstructed sweep. For instance, we packet the point cloud data streams during $[t_{\alpha_2^j}, t_{\alpha_2^{j+1}}]$ to obtain the reconstructed sweep P_i . By this way, the original sweeps S_{j+1} can be re-packing to obtain three reconstructed sweeps (e.g., P_{i-1}, P_i, P_{i+1}). Although the duration of P_i is still 100ms, the time interval between two consecutive reconstructed sweeps (e.g., P_i and P_{i+1}) decreases from 100ms to 33ms. Therefore, our proposed sweep reconstruction can increase the frequency of sweep from 10 Hz to 30 Hz.

V. OUR SYSTEM SR-LIO

A. Overview

Fig. 2 illustrates the framework of our SR-LIO which consists of four main modules: cloud processing, IMU processing, initialization and LIO-optimization. The cloud processing module down-samples the 10 Hz input sweep, then segments and reconstructs the 10 Hz down-sampled sweep to obtain the reconstructed sweep at 30 Hz. The IMU processing module pre-integrates IMU measurements at the same frequency of the reconstructed sweeps (e.g., 30 Hz), and meanwhile calculates

the initial state of the current time. Then it obtains the pre-integration and motion prior which correspond to the reconstructed sweep one by one. The initialization module is used to estimate some state parameters such as gravitational acceleration, accelerometer bias, gyroscope bias, and initial velocity. We provide two initialization schemes (motion initialization and static initialization), where the motion initialization is for handheld devices and the static initialization is for vehicle-mounted devices. The LIO-optimization module performs multi-segment LIO-optimization at 30 Hz to solve all the state variables during the period of a reconstructed sweep. Finally, we add the point clouds to the map and delete the point clouds that are far away. It is noteworthy that if the time interval since the last map update is less than 100ms, we do not update the map to prevent the same point clouds being added to the map repeatedly.

B. Cloud Processing

1) *Down-Sampling*: Due to huge number of 3D point clouds to be processed, the computational burden of the whole system is heavy. In order to reduce the computational burden, we down-sample the input point clouds. Specifically, we put the point clouds of input sweep (i.e., S_j and S_{j+1} in Fig. 3 (a)) into a volume with $0.5 \times 0.5 \times 0.5$ (unit: m) voxel size, and make each voxel contain only one point cloud. This down-sampling strategy ensures that the density distribution of point clouds is uniform in 3D space after down-sampling.

2) *Sweep Segmentation and Reconstruction*: The core idea of sweep reconstruction has been illustrated in Sec. IV. To accommodate different data forms between raw data acquired from LiDAR in practice and that of public datasets, we modify specific processing steps for the two scenarios. Specifically, the point cloud data of public datasets are usually stored as sweep package at 10 Hz. For this kind of data form, the processing steps are illustrated in Fig. 3 (a). To avoid repeated down-sampling operations, we first down-sample the current

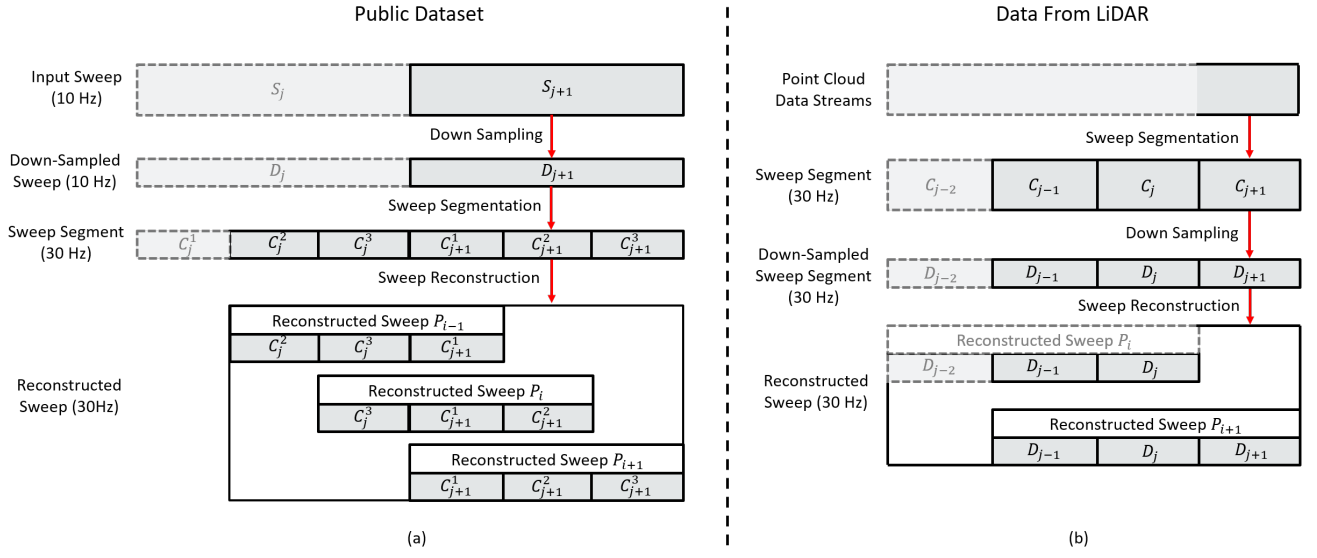


Fig. 3. Illustration of cloud processing which obtains 30 Hz down-sampled reconstructed sweeps. (a) Cloud processing for public datasets, where a new 360deg down-sampled sweep (i.e., D_{j+1}), together with the two segments (i.e., C_j^2, C_j^3) of the last down-sampled sweep (i.e., D_j), are reconstructed to obtain three sweeps (i.e., P_{j-1}, P_j, P_{j+1}). (b) Cloud processing for data from LiDAR, where the sweep segments are captured from the point cloud data streams at 30 Hz. Then the current segment (i.e., C_{j+1}) together with the last two down-sampled segments (i.e., D_{j-1}, D_j), is reconstructed to obtain the reconstructed sweep P_{j+1} .

sweep S_{j+1} to obtain D_{j+1} , then segment D_{j+1} into three segments (i.e., C_{j+1}^1, C_{j+1}^2 and C_{j+1}^3). Finally, each segment (e.g., C_{j+1}^1) together with the two segments (i.e., C_j^2, C_j^3) of the last down-sampled sweep (i.e., D_j), are reconstructed to obtain three reconstructed sweeps (i.e., P_{j-1}, P_j and P_{j+1}). The raw point cloud data from LiDAR sensor are represented as the data stream. For this kind of data form, the processing steps are illustrated in Fig. 3 (b). To avoid repeated down-sampling operations, we first capture sweep segment from raw data stream at 30 Hz, then for the current sweep segment (e.g., C_{j+1}), we down-sample C_{j+1} to obtain D_{j+1} . Finally, D_{j+1} together with the last two down-sampled sweep segments (e.g., D_{j-1}, D_j) to obtain the current reconstructed sweep P_{j+1} .

C. IMU Processing

1) *IMU Pre-Integration*: Typically, the IMU sends out data at a much higher frequency than reconstructed sweeps. Pre-integration of all IMU measurements between two consecutive reconstructed sweeps P_i and P_{i+1} can well summarize the motion of a hardware platform from time t_{e_i} to $t_{e_{i+1}}$, where e_i and e_{i+1} are the end time stamp of P_i and P_{i+1} respectively. In this work, we employ the discrete-time quaternion-based derivation of IMU pre-integration approach [20], [21]. Specifically, the pre-integrations between P_i and P_{i+1} in the corresponding IMU coordinates o_{e_i} and $o_{e_{i+1}}$, i.e., $\hat{\alpha}_{e_{i+1}}^{e_i}, \hat{\beta}_{e_{i+1}}^{e_i}, \hat{\gamma}_{e_{i+1}}^{e_i}$, are calculated, where $\hat{\alpha}_{e_{i+1}}^{e_i}, \hat{\beta}_{e_{i+1}}^{e_i}, \hat{\gamma}_{e_{i+1}}^{e_i}$ are the pre-integration of translation, velocity, rotation from IMU respectively. In addition, the Jacobian of pre-integration with respect to bias, i.e., $\mathbf{J}_{b_a}^\alpha, \mathbf{J}_{b_\omega}^\alpha, \mathbf{J}_{b_a}^\beta, \mathbf{J}_{b_\omega}^\beta$ and $\mathbf{J}_{b_\omega}^\gamma$, are also calculated according to the error state kinematics. The detailed formula of $\alpha_{e_{i+1}}^{e_i}, \beta_{e_{i+1}}^{e_i}, \gamma_{e_{i+1}}^{e_i}$, the covariance matrix $\mathbf{P}_{e_{i+1}}^{e_i}$

and the error state kinematics theory are shown in APPENDIX-I.

Due to the measurement noise (i.e., $\sigma_a^2, \sigma_\omega^2$) and the random walk noise (i.e., $\sigma_{b_a}^2, \sigma_{b_\omega}^2$) in IMU measurements, the pre-integrations (i.e., $\alpha_{e_{i+1}}^{e_i}, \beta_{e_{i+1}}^{e_i}, \gamma_{e_{i+1}}^{e_i}$) inevitably introduces errors. A longer time interval between t_{e_i} and $t_{e_{i+1}}$ will involve more IMU measurements in pre-integrations, and hence produce greater cumulative error. After the proposed sweep reconstruction, the time interval between two consecutive sweeps is reduced from 100ms to 33ms, which significantly reduces the cumulative error of pre-integration.

2) *State Prediction*: When every new reconstructed sweep P_{i+1} completes, we use IMU measurements to predict the state at the beginning time stamp of P_{i+1} (i.e., $\mathbf{x}_{b_{i+1}}^w$) and the state at the end time stamp of P_{i+1} (i.e., $\mathbf{x}_{e_{i+1}}^w$) to provide the prior motion for LIO-optimization. Specifically, the predicted state $\mathbf{x}_{b_{i+1}}^w$ (i.e., $\mathbf{t}_{b_{i+1}}^w, \mathbf{R}_{b_{i+1}}^w, \mathbf{v}_{b_{i+1}}^w, \mathbf{b}_{a_{b_{i+1}}}, \mathbf{b}_{\omega_{b_{i+1}}}$) is assigned as:

$$\mathbf{x}_{b_{i+1}}^w = \mathbf{x}_{e_{i-2}}^w \quad (6)$$

and $\mathbf{x}_{e_{i+1}}^w$ (i.e., $\mathbf{t}_{e_{i+1}}^w, \mathbf{R}_{e_{i+1}}^w, \mathbf{v}_{e_{i+1}}^w, \mathbf{b}_{a_{e_{i+1}}}, \mathbf{b}_{\omega_{e_{i+1}}}$) is calculated as:

$$\begin{aligned} \mathbf{R}_{n+1}^w &= \mathbf{R}_n^w \text{Exp} \left(\left(\frac{\hat{\omega}_n + \hat{\omega}_{n+1}}{2} - \mathbf{b}_{\omega_{e_i}} \right) \delta t \right) \\ \mathbf{v}_{n+1}^w &= \mathbf{v}_n^w + \left(\frac{\hat{\mathbf{a}}_n + \hat{\mathbf{a}}_{n+1}}{2} - \mathbf{b}_{a_{e_i}} - \mathbf{R}_n^w \mathbf{g}^w \right) \delta t \\ \mathbf{t}_{n+1}^w &= \mathbf{t}_n^w + \mathbf{v}_n^w \delta t + \frac{1}{2} \left(\frac{\hat{\mathbf{a}}_n + \hat{\mathbf{a}}_{n+1}}{2} - \mathbf{b}_{a_{e_i}} - \mathbf{R}_n^w \mathbf{g}^w \right) \delta t^2 \end{aligned} \quad (7)$$

where \mathbf{g}^w is the gravitational acceleration in the world coordinates, n and $n+1$ are two time instants of obtaining an IMU measurement during $[t_{e_i}, t_{e_{i+1}}]$, δt is the time interval between n and $n+1$. We iteratively increase n from 0 to

$(t_{e_{i+1}} - t_{e_i})/\delta t$ to obtain $\mathbf{x}_{e_{i+1}}^w$. When $n = 0$, $\mathbf{x}_n^w = \mathbf{x}_{e_i}^w$. For $\mathbf{b}_{\mathbf{a}_{e_{i+1}}}$ and $\mathbf{b}_{\boldsymbol{\omega}_{e_{i+1}}}$, we set the predicted values of them by: $\mathbf{b}_{\mathbf{a}_{e_{i+1}}} = \mathbf{b}_{\mathbf{a}_{e_i}}$ and $\mathbf{b}_{\boldsymbol{\omega}_{e_{i+1}}} = \mathbf{b}_{\boldsymbol{\omega}_{e_i}}$.

D. Motion Initialization

The initialization module aims to estimate all necessary values including initial pose, velocity, gravitational acceleration, accelerometer bias and gyroscope bias, for state prediction and subsequent LIO-optimization. The motion initialization method proposed in VINs-Mono [20] is suitable for cases where all three axes (i.e., X-Y-Z) contain sufficient motion excitation. This requirement can be easily met on handheld devices. Therefore, we modify the original initialization method of VINs-Mono to adapt it to our SR-LIO, for initialization on the handheld device. Different from VINs-Mono which calculates the poses between the oldest and the newest frame in the sliding window through the essential matrix, and compute the depth of 2D pixels without metric scale via triangulation, we directly obtain the initial map with metric scale from the LiDAR point clouds, and calculate the pose by ICP. In addition, we omit the scale initialization step in VINs-Mono as we can directly obtain it from both LiDAR and IMU.

1) *Map Initialization*: Before initialization successfully, we utilize the down-sampled reconstructed sweep from the cloud processing module to perform LiDAR-only ICP for pose solution. The specific formulas of ICP and consistency constraints are illustrated in Sec. V-F1, while a total of 20 consecutive reconstructed sweeps are estimated in this way. After pose solution, the point clouds of the first sweep are added into the volume, and each voxel contains a maximum of 20 point clouds. Then the point clouds of other sweeps are selectively added to the volume in a chronological order. The selection strategy is detailed in Sec. V-F2. After above steps, the map initialization is finished.

2) *Gyroscope Bias Initialization*: Considering two consecutive reconstructed sweeps P_i and P_{i+1} in the first 20 reconstructed sweeps, we obtain rotation $\mathbf{q}_{e_i}^{e_0}$ and $\mathbf{q}_{e_{i+1}}^{e_0}$ from LiDAR-only pose estimation, as well as the relative rotation constraint $\hat{\gamma}_{e_{i+1}}^{e_i}$ from IMU pre-integrations. We linearize the IMU pre-integration terms with respect to the gyroscope bias and minimize the following cost function:

$$\min_{\delta \mathbf{b}_{\boldsymbol{\omega}}} \sum_{i=0}^{19} \left\| \mathbf{q}_{e_{i+1}}^{e_0}{}^{-1} \otimes \mathbf{q}_{e_i}^{e_0} \otimes \gamma_{e_{i+1}}^{e_i} \right\|^2 \quad (8)$$

$$\gamma_{e_{i+1}}^{e_i} \approx \hat{\gamma}_{e_{i+1}}^{e_i} \otimes \begin{bmatrix} 1 \\ \frac{1}{2} \mathbf{J}_{\mathbf{b}_{\boldsymbol{\omega}}}^{\gamma} \delta \mathbf{b}_{\boldsymbol{\omega}} \end{bmatrix}$$

where $\mathbf{J}_{\mathbf{b}_{\boldsymbol{\omega}}}^{\gamma}$ is derived in Appendix-I. We obtain $\delta \mathbf{b}_{\boldsymbol{\omega}}$ according to Eq. 8 and add it to the original $\mathbf{b}_{\boldsymbol{\omega}} = \mathbf{0}$ to get an initial estimation of the gyroscope bias $\mathbf{b}_{\boldsymbol{\omega}}$. Then we re-propagate all IMU pre-integration terms $\hat{\alpha}_{e_{i+1}}^{e_i}$, $\hat{\beta}_{e_{i+1}}^{e_i}$ and $\hat{\gamma}_{e_{i+1}}^{e_i}$ using the new gyroscope bias.

3) *Initial Velocity and Gravity Initialization*: After the gyroscope bias is initialized, we proceed to initialize the velocity and the gravitational acceleration, where the vector of variables is written as:

$$\mathbf{x}_I = [\mathbf{v}_{e_0}^{e_0}, \mathbf{v}_{e_1}^{e_1}, \dots, \mathbf{v}_{e_{19}}^{e_{19}}, \mathbf{g}^{e_0}]^T \quad (9)$$

where $\mathbf{v}_{e_i}^{e_i}$ is the velocity in the IMU coordinates when the i_{th} sweep finishes, and \mathbf{g}^{e_0} is the gravitational acceleration when completes the first reconstructed sweep P_0 .

Considering two consecutive reconstructed sweeps P_i and P_{i+1} in initialization, we calculate Eq. 10 as follow:

$$\alpha_{e_{i+1}}^{e_i} = \mathbf{R}_{e_0}^{e_i} \left(\mathbf{t}_{e_{i+1}}^{e_0} - \mathbf{t}_{e_i}^{e_0} + \frac{1}{2} \mathbf{g}^{e_0} \Delta t^2 - \mathbf{R}_{e_i}^{e_0} \mathbf{v}_{e_i}^{e_i} \Delta t \right) \quad (10)$$

$$\beta_{e_{i+1}}^{e_i} = \mathbf{R}_{e_0}^{e_i} \left(\mathbf{R}_{e_{i+1}}^{e_0} \mathbf{v}_{e_{i+1}}^{e_{i+1}} + \mathbf{g}^{e_0} \Delta t - \mathbf{R}_{e_i}^{e_0} \mathbf{v}_{e_i}^{e_i} \right)$$

where Δt is the time interval between two consecutive reconstructed sweeps. Combining Eq. 10 and 29 (in the Appendix-I) into the following linear measurement model, we can get:

$$\hat{\mathbf{z}}_{e_{i+1}}^{e_i} = \begin{bmatrix} \hat{\alpha}_{e_{i+1}}^{e_i} - \mathbf{R}_{e_0}^{e_i} (\mathbf{t}_{e_{i+1}}^{e_0} - \mathbf{t}_{e_i}^{e_0}) \\ \hat{\beta}_{e_{i+1}}^{e_i} \end{bmatrix} = \mathbf{H}_{e_{i+1}}^{e_i} \mathbf{x}_{sub} + \mathbf{n}_{e_{i+1}}^{e_i} \quad (11)$$

where

$$\mathbf{H}_{e_{i+1}}^{e_i} = \begin{bmatrix} -\mathbf{I} \Delta t & \mathbf{0} & \frac{1}{2} \mathbf{R}_{e_0}^{e_i} \Delta t^2 \\ -\mathbf{I} & \mathbf{R}_{e_0}^{e_i} \mathbf{R}_{e_{i+1}}^{e_0} & \mathbf{R}_{e_0}^{e_i} \Delta t \end{bmatrix} \quad (12)$$

$$\mathbf{x}_{sub} = [\mathbf{v}_{e_i}^{e_i}, \mathbf{v}_{e_{i+1}}^{e_{i+1}}, \mathbf{g}^{e_0}]^T$$

By solving the following linear least square problem:

$$\min_{\mathbf{x}_I} \sum_{i=0}^{19} \left\| \hat{\mathbf{z}}_{e_{i+1}}^{e_i} - \mathbf{H}_{e_{i+1}}^{e_i} \mathbf{x}_{sub} \right\|^2 \quad (13)$$

we can get velocities for every reconstructed sweep, as well as the gravitational acceleration in the coordinates of first sweep $(\cdot)^{e_0}$. Finally, we utilize [20] to further refine the gravitational acceleration by constraining the magnitude.

E. Static Initialization

The static initialization method was proposed in Open-VINs [22], which is suitable for cases where the device remains stationary for a short period at first. This requirement is easily met on the vehicle-mounted device, where a car usually starts motion from static.

1) *Gyroscope Bias Initialization*: Since the vehicle platform remains stationary, the gyroscope measurement is the vector sum of gyroscope bias $\mathbf{b}_{\boldsymbol{\omega}}$ and measurement noise $\mathbf{n}_{\boldsymbol{\omega}}$. As described in Sec. III-C, the noise of gyroscope measurement is modeled as $\mathbf{n}_{\boldsymbol{\omega}} \sim N(\mathbf{0}, \sigma_{\boldsymbol{\omega}}^2)$. Therefore, when we average the gyroscope measurements $\bar{\boldsymbol{\omega}}_t$ over a period of time, the average of $\mathbf{n}_{\boldsymbol{\omega}}$ should be zero, and the value of $\bar{\boldsymbol{\omega}}_t$ is equal to the gyroscope bias.

2) *Gravity and Accelerometer Bias Initialization*: Since the vehicle platform remains stationary, the accelerometer measurement is the vector sum of accelerometer bias $\mathbf{b}_{\mathbf{a}}$, measurement noise $\mathbf{n}_{\mathbf{a}}$ and the gravitational acceleration \mathbf{g} . As described in Sec. III-C, the noise of accelerometer measurement is modeled as $\mathbf{n}_{\mathbf{a}} \sim N(\mathbf{0}, \sigma_{\mathbf{a}}^2)$. By averaging the accelerometer measurements $\bar{\mathbf{a}}_t$ over a period of time, the average of $\mathbf{n}_{\mathbf{a}}$ should be zero, and the value of $\bar{\mathbf{a}}_t$ is equal to the vector sum of $\mathbf{b}_{\mathbf{a}}$ and the gravitational acceleration \mathbf{g} . In general, the value of $\mathbf{b}_{\mathbf{a}}$ is much smaller than \mathbf{g} (e.g., $|\mathbf{b}_{\mathbf{a}}| = 0.01|\mathbf{g}|$). Therefore, we approximate the direction of vector $\bar{\mathbf{a}}_t$ as the direction of gravity. On the other hand, the

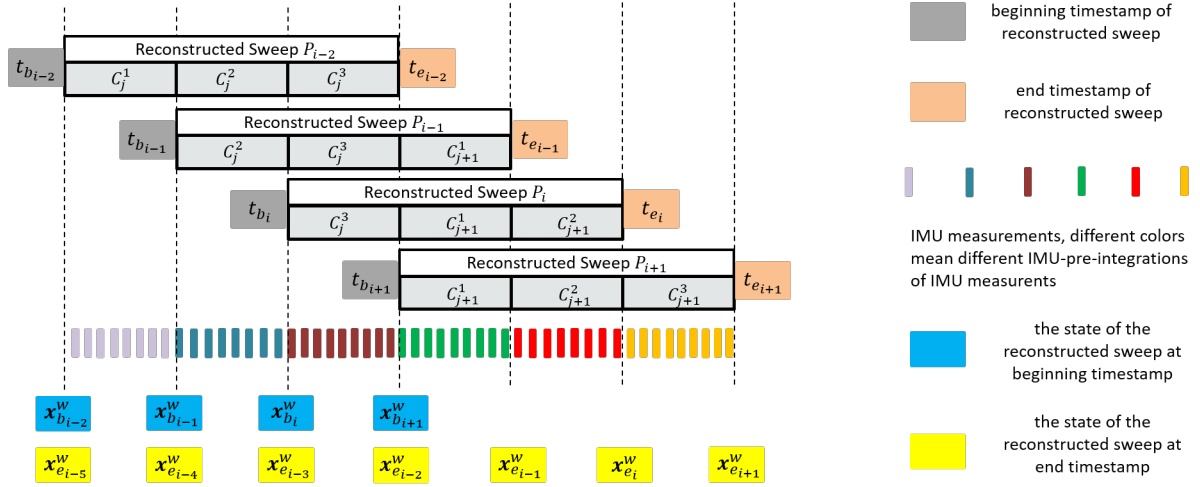


Fig. 4. Illustration of multi-segment LIO-optimization, which aims to optimize the variables (e.g., $\mathbf{x}_{b_{i+1}}^w$, $\mathbf{x}_{e_{i-1}}^w$, $\mathbf{x}_{e_i}^w$, $\mathbf{x}_{e_{i+1}}^w$) during the period (e.g., $[t_{b_{i+1}}, t_{e_{i+1}}]$) of a current reconstructed sweep P_{i+1} . Our method enable the states of each sweep segment (e.g., $\mathbf{x}_{b_{i+1}}^w$ and $\mathbf{x}_{e_{i-1}}^w$ for C_{j+1}^1 , $\mathbf{x}_{e_{i-1}}^w$ and $\mathbf{x}_{e_i}^w$ for C_{j+1}^2 , $\mathbf{x}_{e_i}^w$ and $\mathbf{x}_{e_{i+1}}^w$ for C_{j+1}^3) to be constrained by both pre-integrated IMU measurements (e.g., green, red, orange rectangles) and LiDAR point-to-plane residuals.

value of the gravitational acceleration (i.e., G) can be obtained directly from the latitude and longitude of our position on the earth. Therefore, the gravitational acceleration in the world coordinates $(\cdot)^w$ is calculated as:

$$\mathbf{g}^w = \frac{\bar{\mathbf{a}}_t}{|\bar{\mathbf{a}}_t|} G \quad (14)$$

Then the accelerometer bias \mathbf{b}_a is calculated as:

$$\mathbf{b}_a = \bar{\mathbf{a}}_t - \mathbf{g}^w \quad (15)$$

F. LIO-Optimization

1) *Multi-Segment LIO Optimization*: LIO-optimization aims to utilize data from both LiDAR and IMU to refine the state variables during the period (i.e., $[t_{b_{i+1}}, t_{e_{i+1}}]$) of the current reconstructed sweep P_{i+1} . As illustrated in Fig. 4, the variables during $[t_{b_{i+1}}, t_{e_{i+1}}]$ are $\mathbf{x}_{b_{i+1}}^w$, $\mathbf{x}_{e_{i-1}}^w$, $\mathbf{x}_{e_i}^w$, $\mathbf{x}_{e_{i+1}}^w$, which are the states at $t_{b_{i+1}}$, $t_{e_{i-1}}$, t_{e_i} and $t_{e_{i+1}}$ respectively. There are three IMU pre-integrations during $[t_{b_{i+1}}, t_{e_{i+1}}]$, which are collected from the IMU measurements denoted by the green rectangles, the red rectangles and the orange rectangles in Fig. 4 respectively. The pre-integrated IMU measurements between $[t_{b_{i+1}}, t_{e_{i-1}}]$ (i.e., green rectangles) constrain the state $\mathbf{x}_{b_{i+1}}^w$ and $\mathbf{x}_{e_{i-1}}^w$, the pre-integrated IMU measurements between $[t_{e_{i-1}}, t_{e_i}]$ (i.e., red rectangles) constrain the state $\mathbf{x}_{e_{i-1}}^w$ and $\mathbf{x}_{e_i}^w$, and the pre-integrated IMU measurements between $[t_{e_i}, t_{e_{i+1}}]$ (i.e., orange rectangles) constrain the state $\mathbf{x}_{e_i}^w$ and $\mathbf{x}_{e_{i+1}}^w$. Meanwhile, for a point cloud \mathbf{p} collected at time t_p ($t_p \in [t_{b_{i+1}}, t_{e_{i+1}}]$), we can build the ICP constraint for \mathbf{p} as a function of $\mathbf{x}_{b_{i+1}}^w$ and $\mathbf{x}_{e_{i-1}}^w$. Similarly, for every point cloud collected at $[t_{e_{i-1}}, t_{e_i}]$ or $[t_{e_i}, t_{e_{i+1}}]$, the ICP constraint for it can be represented as a function of $\{\mathbf{x}_{e_{i-1}}^w, \mathbf{x}_{e_i}^w\}$ or $\{\mathbf{x}_{e_i}^w, \mathbf{x}_{e_{i+1}}^w\}$. By this way, all variables during $[t_{b_{i+1}}, t_{e_{i+1}}]$:

$$\chi = \{\mathbf{x}_{b_{i+1}}^w, \mathbf{x}_{e_{i-1}}^w, \mathbf{x}_{e_i}^w, \mathbf{x}_{e_{i+1}}^w\} \quad (16)$$

can be constrained by the observations from IMU and LiDAR. Since we consider a reconstructed sweep as three sweep segments (i.e., C_{j+1}^1 , C_{j+1}^2 , C_{j+1}^3), and optimize the states at the beginning and the end of each segment. Therefore, we name our approach as “multi-segment LIO-optimization”. In the following, we explain the constraints from LiDAR, IMU and consistency in detail.

The residual from the LiDAR constraint. For a point cloud \mathbf{p} , we first find to which segment \mathbf{p} belongs. For ease of description, we assume \mathbf{p} belongs to segment C_{j+1}^1 which begins at $t_{b_{i+1}}$ and ends at $t_{e_{i+1}}$. Specially, we first project \mathbf{p} to the world coordinates to obtain \mathbf{p}^w , and then find 20 nearest point clouds around \mathbf{p}^w from the volume. To search for the nearest neighbor of \mathbf{p}^w , we only search in the voxel V to which \mathbf{p}^w belongs, and the 8 voxels adjacent to V . The 20 nearest point clouds are used to fit a plane with the normal \mathbf{n} and the distance d . Accordingly, we can build the point-to-plane residual r^p for \mathbf{p} as:

$$\begin{aligned} r^p &= \omega_p (\mathbf{n}^T \mathbf{p}^w + d) \\ \mathbf{p}^w &= \mathbf{q}_p^w \mathbf{p} + \mathbf{t}_p^w \\ \alpha &= \frac{t_p - t_{b_{i+1}}}{t_{e_{i-1}} - t_{b_{i+1}}} \\ \mathbf{t}_p^w &= (1 - \alpha) \mathbf{t}_{b_{i+1}}^w + \alpha \mathbf{t}_{e_{i-1}}^w \\ \mathbf{q}_p^w &= \mathbf{q}_{b_{i+1}}^w \cdot \text{slerp}(\alpha, \mathbf{q}_{e_{i-1}}^w) \end{aligned} \quad (17)$$

where ω_p is a weight parameter defined by [5], $\mathbf{q}_{b_{i+1}}^w$ and $\mathbf{q}_{e_{i-1}}^w$ are the rotation with respect to $(\cdot)^w$ at $t_{b_{i+1}}$ and $t_{e_{i-1}}$ respectively, $\mathbf{t}_{b_{i+1}}^w$ and $\mathbf{t}_{e_{i-1}}^w$ are the translation with respect to $(\cdot)^w$ at $t_{b_{i+1}}$ and $t_{e_{i-1}}$ respectively. Both $\mathbf{q}_{b_{i+1}}^w$, $\mathbf{q}_{e_{i-1}}^w$, $\mathbf{t}_{b_{i+1}}^w$, $\mathbf{t}_{e_{i-1}}^w$ are variables to be refined, and the initial value of $\mathbf{q}_{b_{i+1}}^w$ and $\mathbf{t}_{b_{i+1}}^w$ are obtained from the prior motion from Sec. V-C2, the initial value of $\mathbf{q}_{e_{i-1}}^w$ and $\mathbf{t}_{e_{i-1}}^w$ are the results of the previous LIO-optimization.

However, only building the LiDAR constraint for \mathbf{p} as a function of $\mathbf{x}_{b_{i+1}}^w$ and $\mathbf{x}_{e_{i-1}}^w$ is unreliable because C_{j+1}^1 is not a full 360deg sweep, which greatly reduces the accuracy of ICP solution. Therefore, we build an additional point-to-plane residual $r_a^{\mathbf{p}}$ for \mathbf{p} as a function of $\mathbf{x}_{b_{i+1}}^w$ and $\mathbf{x}_{e_{i+1}}^w$, where $\mathbf{x}_{b_{i+1}}^w$ and $\mathbf{x}_{e_{i+1}}^w$ are the beginning state and the end state of a full 360deg sweep:

$$\begin{aligned} r_a^{\mathbf{p}} &= \omega_{\mathbf{p}} (\mathbf{n}^T \mathbf{p}^w + d) \\ \mathbf{p}^w &= \mathbf{q}_{\mathbf{p}} \mathbf{p} + \mathbf{t}_{\mathbf{p}}^w \\ \alpha &= \frac{t_{\mathbf{p}} - t_{b_{i+1}}}{t_{e_{i+1}} - t_{b_{i+1}}} \\ \mathbf{t}_{\mathbf{p}}^w &= (1 - \alpha) \mathbf{t}_{b_{i+1}}^w + \alpha \mathbf{t}_{e_{i+1}}^w \\ \mathbf{q}_{\mathbf{p}} &= \mathbf{q}_{b_{i+1}}^w .slerp(\alpha, \mathbf{q}_{e_{i+1}}^w) \end{aligned} \quad (18)$$

where $r_a^{\mathbf{p}}$ is an additional residual which is related to variables $\mathbf{q}_{b_{i+1}}^w, \mathbf{q}_{e_{i+1}}^w, \mathbf{t}_{b_{i+1}}^w, \mathbf{t}_{e_{i+1}}^w$. By this way, for an arbitrary point \mathbf{p} , we can build two residuals (e.g., $r^{\mathbf{p}}$ and $r_a^{\mathbf{p}}$) to optimize six or eight variables, i.e., $\mathbf{q}_{b_{i+1}}^w, \mathbf{q}_{e_{i-1}}^w, \mathbf{q}_{e_i}^w, \mathbf{q}_{e_{i+1}}^w, \mathbf{t}_{b_{i+1}}^w, \mathbf{t}_{e_{i-1}}^w, \mathbf{t}_{e_i}^w$ and $\mathbf{t}_{e_{i+1}}^w$. The Jacobian of the point-to-plane residual about the rotation and translation is detailed in Appendix-II.

The residual from the IMU constraint. There are three sweep segments (i.e., $C_{j+1}^1, C_{j+1}^2, C_{j+1}^3$) during $[t_{b_{i+1}}, t_{e_{i+1}}]$, and each segment can provide an IMU pre-integration to constrain the state at the beginning and the end of a sweep segment. For instance, considering the IMU measurements during $[t_{e_i}, t_{e_{i+1}}]$, according to pre-integration introduced in Sec. V-C1, the residual for pre-integrated IMU measurements can be computed as:

$$\mathbf{r}_{o_{e_{i+1}}}^{e_i} = \begin{bmatrix} \mathbf{R}_{e_i}^{e_{i+1}} (\mathbf{t}_{e_{i+1}}^w - \mathbf{t}_{e_i}^w + \frac{1}{2} \mathbf{g}^w \Delta t^2 - \mathbf{v}_{e_i}^w \Delta t) - \hat{\alpha}_{e_{i+1}}^{e_i} \\ \mathbf{R}_{e_i}^{e_{i+1}} (\mathbf{v}_{e_{i+1}}^w + \mathbf{g}^w \Delta t - \mathbf{v}_{e_i}^w) - \hat{\beta}_{e_{i+1}}^{e_i} \\ 2 \left[\mathbf{q}_{e_i}^{w-1} \otimes \mathbf{q}_{e_{i+1}}^w \otimes (\hat{\gamma}_{e_{i+1}}^{e_i})^{-1} \right]_{xyz} \\ \mathbf{b}_{a_{e_{i+1}}} - \mathbf{b}_{a_{e_i}} \\ \mathbf{b}_{\omega_{e_{i+1}}} - \mathbf{b}_{\omega_{e_i}} \end{bmatrix} \quad (19)$$

where $[\cdot]_{xyz}$ extracts the vector part of a quaternion \mathbf{q} for error state representation. Similarly, the residual for pre-integrated IMU measurements during $[t_{b_{i+1}}, t_{e_{i-1}}]$ and $[t_{e_{i-1}}, t_{e_i}]$ can be computed as:

$$\mathbf{r}_{o_{e_{i-1}}}^{b_{i+1}} = \begin{bmatrix} \mathbf{R}_{e_{i-1}}^{b_{i+1}} (\mathbf{t}_{e_{i-1}}^w - \mathbf{t}_{b_{i+1}}^w + \frac{1}{2} \mathbf{g}^w \Delta t^2 - \mathbf{v}_{b_{i+1}}^w \Delta t) - \hat{\alpha}_{e_{i-1}}^{b_{i+1}} \\ \mathbf{R}_{e_{i-1}}^{b_{i+1}} (\mathbf{v}_{e_{i-1}}^w + \mathbf{g}^w \Delta t - \mathbf{v}_{b_{i+1}}^w) - \hat{\beta}_{e_{i-1}}^{b_{i+1}} \\ 2 \left[\mathbf{q}_{b_{i+1}}^{w-1} \otimes \mathbf{q}_{e_{i-1}}^w \otimes (\hat{\gamma}_{e_{i-1}}^{b_{i+1}})^{-1} \right]_{xyz} \\ \mathbf{b}_{a_{e_{i-1}}} - \mathbf{b}_{a_{b_{i+1}}} \\ \mathbf{b}_{\omega_{e_{i-1}}} - \mathbf{b}_{\omega_{b_{i+1}}} \end{bmatrix} \quad (20)$$

$$\mathbf{r}_{o_{e_i}}^{e_{i-1}} = \begin{bmatrix} \mathbf{R}_{e_{i-1}}^{e_i} (\mathbf{t}_{e_i}^w - \mathbf{t}_{e_{i-1}}^w + \frac{1}{2} \mathbf{g}^w \Delta t^2 - \mathbf{v}_{e_{i-1}}^w \Delta t) - \hat{\alpha}_{e_i}^{e_{i-1}} \\ \mathbf{R}_{e_{i-1}}^{e_i} (\mathbf{v}_{e_i}^w + \mathbf{g}^w \Delta t - \mathbf{v}_{e_{i-1}}^w) - \hat{\beta}_{e_i}^{e_{i-1}} \\ 2 \left[\mathbf{q}_{e_{i-1}}^{w-1} \otimes \mathbf{q}_{e_i}^w \otimes (\hat{\gamma}_{e_i}^{e_{i-1}})^{-1} \right]_{xyz} \\ \mathbf{b}_{a_{e_i}} - \mathbf{b}_{a_{e_{i-1}}} \\ \mathbf{b}_{\omega_{e_i}} - \mathbf{b}_{\omega_{e_{i-1}}} \end{bmatrix} \quad (21)$$

At the end of each iteration of LIO joint optimization, we utilize Eq. 29 to update $\hat{\alpha}_{e_{i-1}}^{b_{i+1}}, \hat{\alpha}_{e_i}^{e_{i-1}}, \hat{\alpha}_{e_{i+1}}^{e_i}, \hat{\beta}_{e_{i-1}}^{b_{i+1}}, \hat{\beta}_{e_i}^{e_{i-1}}, \hat{\beta}_{e_{i+1}}^{e_i}, \hat{\gamma}_{e_{i-1}}^{b_{i+1}}, \hat{\gamma}_{e_i}^{e_{i-1}}$ and $\hat{\gamma}_{e_{i+1}}^{e_i}$. The Jacobian of the IMU residual about the state variables is detailed in Appendix-III.

The residual from the consistency constraint. As illustrated in Fig. 4, there are two states (i.e., $\mathbf{x}_{e_{i-2}}^w$ and $\mathbf{x}_{b_{i+1}}^w$) at the time stamp $t_{b_{i+1}} (t_{e_{i-2}})$. Logically, $\mathbf{x}_{e_{i-2}}^w$ and $\mathbf{x}_{b_{i+1}}^w$ should be the same. Therefore, we build the consistency residual as follow:

$$\mathbf{r}_c = \begin{bmatrix} \mathbf{r}_c^{\mathbf{t}} \\ \mathbf{r}_c^{\mathbf{q}} \\ \mathbf{r}_c^{\mathbf{v}} \\ \mathbf{r}_c^{\mathbf{b}_a} \\ \mathbf{r}_c^{\mathbf{b}_\omega} \end{bmatrix} = \begin{bmatrix} \mathbf{t}_{b_{i+1}}^w - \mathbf{t}_{e_{i-2}}^w \\ 2 \left[\mathbf{q}_{e_{i-2}}^{w-1} \otimes \mathbf{q}_{b_{i+1}}^w \right]_{xyz} \\ \mathbf{v}_{b_{i+1}}^w - \mathbf{v}_{e_{i-2}}^w \\ \mathbf{b}_{a_{b_{i+1}}} - \mathbf{b}_{a_{e_{i-2}}} \\ \mathbf{b}_{\omega_{b_{i+1}}} - \mathbf{b}_{\omega_{e_{i-2}}} \end{bmatrix} \quad (22)$$

where $\mathbf{t}_{b_{i+1}}^w, \mathbf{q}_{b_{i+1}}^w, \mathbf{b}_{a_{b_{i+1}}}$ and $\mathbf{b}_{\omega_{b_{i+1}}}$ are variables to be optimized. The Jacobian of the consistency residual about the $\mathbf{t}_{b_{i+1}}^w, \mathbf{q}_{b_{i+1}}^w, \mathbf{b}_{a_{b_{i+1}}}$ and $\mathbf{b}_{\omega_{b_{i+1}}}$ is detailed in Appendix-IV.

By minimizing the sum of point-to-plane residuals, the IMU pre-integration residuals and the consistency residuals, we obtain a maximum posteriori estimation as:

$$\chi = \min_{\chi} \left\{ \rho \left(\sum_{\mathbf{p} \in P_{i+1}} \|r^{\mathbf{p}}\|_{\mathbf{P}_L}^2 + \sum_{\mathbf{p} \in P_{i+1}} \|r_a^{\mathbf{p}}\|_{\mathbf{P}_L}^2 + \left\| \mathbf{r}_{o_{e_{i-1}}}^{b_{i+1}} \right\|_{\mathbf{P}_{e_{i-1}}^{b_{i+1}}}^2 + \left\| \mathbf{r}_{o_{e_i}^{e_{i-1}}} \right\|_{\mathbf{P}_{e_i}^{e_{i-1}}}^2 + \left\| \mathbf{r}_{o_{e_{i+1}}^{e_i}} \right\|_{\mathbf{P}_{e_{i+1}}^{e_i}}^2 + \left\| \mathbf{r}_c \right\|^2 \right) \right\} \quad (23)$$

where ρ is the Huber kernel to eliminate the influence of outlier residuals. $\mathbf{P}_{e_{i-1}}^{b_{i+1}}, \mathbf{P}_{e_i}^{e_{i-1}}, \mathbf{P}_{e_{i+1}}^{e_i}$ are the covariance matrix of pre-integrated IMU measurements, which are introduced in Appendix-I. The inverse of $\mathbf{P}_{e_{i-1}}^{b_{i+1}}, \mathbf{P}_{e_i}^{e_{i-1}}, \mathbf{P}_{e_{i+1}}^{e_i}$ are utilized as the weight of IMU pre-integration residuals. \mathbf{P}_L is a constant (e.g., 0.001 in our system) to indicate the reliability of the point-to-plane residuals. The inverse of \mathbf{P}_L is utilized as the weight of point-to-plane residuals. After finishing LIO joint optimization, we selectively add the point cloud of current reconstructed sweep to the volume map.

2) Map Update with Frequency Control: The cloud map is stored in a volume, and the size of each voxel is $1.0 \times 1.0 \times 1.0$ (unit: m). Each voxel contains a maximum of 20 point clouds. If a voxel already has 20 point clouds, the new point clouds cannot be added to it.

As illustrated in Fig. 4, the consecutive two reconstructed sweeps have two common sweep segments. For instance, both P_i and P_{i+1} have the segment C_{j+1}^1 and C_{j+1}^2 . If we add the point cloud of each reconstructed sweep to the volume,

TABLE I
DATASETS FOR EVALUATION

	spinning LiDAR		IMU	
	Line	Rate	Type	Rate
<i>nclt</i>	32	7 Hz	9-axis	100 Hz
<i>utbm</i>	32	10 Hz	6-axis	100 Hz
<i>ulhk</i>	32	10 Hz	9-axis	100 Hz

the point clouds in common sweep segments would be added repeatedly. To avoid this problem, we perform map update at 10 Hz. For instance, if the current sweep to be added is P_{i-2} , the next sweep to be added is P_{i+1} , which does not share common sweep segments with P_{i-2} . After adding new point clouds to the volume, we delete the point clouds that are far away from the current position.

VI. EXPERIMENTS

We evaluated our SR-LIO on both the public datasets *nclt* [23], *utbm* [24] and *ulhk* [25]. *nclt* is a large-scale, long-term autonomous unmanned ground vehicle dataset collected in the University of Michigan's North Campus. The *nclt* dataset contains a full data stream from a Velodyne HDL-32E LiDAR and 50 Hz data from Microstrain MS25 IMU. The *nclt* dataset has a much longer duration and amount of data than other datasets and contains several open scenes, such as a large open parking lot. Different from the other two datasets (i.e., *utbm* and *ulhk*), the LiDAR of *nclt* takes 130~140ms to complete a 360deg sweep (i.e., the frequency of a sweep is about 7 Hz). In addition, at the end of some sequences of *nclt*, the Segway vehicle platform enters a long indoor corridor through a door from the outdoor scene, yielding significant scene changes. This large differences in scenes produce great difficulties for ICP point cloud registration, and hence almost all systems would break down here. Therefore, we omit the test for these cases which usually locate at the end of the sequences. In addition, 50 Hz IMU measurements cannot meet the requirements of some systems (e.g., LIO-SAM [14]). Therefore, we increase the frequency of the IMU to 100 Hz by interpolation.

The *utbm* dataset is collected with a human-driving robocar runs at a maximum 50 km/h speed. The robocar has two 10 Hz Velodyne HDL-32E and 100 Hz Xsens MTi-28A53G25 IMU. For point clouds, we only utilize the data from the left LiDAR. The *ulhk* dataset contains 10 Hz LiDAR sweep from Velodyne HDL-32E LiDAR5 and 100 Hz IMU data from the nine-axis Xsens MTi-10 IMU. All the sequences of *utbm* and *ulhk* are collected in structured urban areas by a human-driving vehicle. The datasets' information, including the sensors' type and data rate, are illustrated in Table I. As all three datasets utilize the vehicle platform, we employ static initialization in our system. Details of all the 22 sequences used in this section, including name, duration, and distance, are listed in Table II. For all three datasets, we utilize the universal evaluation metrics – absolute translational error (ATE) as the evaluation metrics. A consumer-level computer equipped with an Intel Core i7-12700 and 32 GB RAM is used for all experiments.

TABLE II
DATASETS OF ALL SEQUENCES FOR EVALUATION

Abbreviation	Name	Duration (min : sec)	Distance (km)
<i>nclt_1</i>	2012-01-08	93:53	6.60
<i>nclt_2</i>	2012-01-15	111:46	4.01
<i>nclt_3</i>	2012-02-02	98:37	6.45
<i>nclt_4</i>	2012-04-29	43:17	1.86
<i>nclt_5</i>	2012-05-11	84:32	3.13
<i>nclt_6</i>	2012-06-15	55:10	1.62
<i>nclt_7</i>	2012-12-01	75:50	2.27
<i>nclt_8</i>	2013-01-10	17:02	0.26
<i>nclt_9</i>	2013-04-05	69:06	1.40
<i>utbm_1</i>	2018-07-19	15:26	4.98
<i>utbm_2</i>	2019-01-31	16:00	6.40
<i>utbm_3</i>	2019-04-18	11:59	5.11
<i>utbm_4</i>	2018-07-20	16:45	4.99
<i>utbm_5</i>	2018-07-17	15:59	4.99
<i>utbm_6</i>	2018-07-16	15:59	4.99
<i>utbm_7</i>	2018-07-13	16:59	5.03
<i>ulhk_1</i>	HK-Data-2019-01-17	5:18	0.60
<i>ulhk_2</i>	HK-Data-2019-03-16-1	2:55	0.23
<i>ulhk_3</i>	HK-Data-2019-03-17	5:18	0.62
<i>ulhk_4</i>	HK-Data-2019-04-26-1	2:30	0.55
<i>ulhk_5</i>	HK-Data-2019-04-26-2	4:20	0.74

TABLE III
ATE COMPARISON OF STATE-OF-THE-ARTS

	LiLi-OM [11]	LIO-SAM [14]	LINs [13]	Fast-LIO2 [16]	Ours
<i>nclt_1</i>	50.71	x	x	3.57	1.55
<i>nclt_2</i>	309.79	2.14	x	1.74	1.53
<i>nclt_3</i>	91.86	7.18	x	2.00	1.57
<i>nclt_4</i>	93.61	1.75	x	1.40	1.22
<i>nclt_5</i>	185.24	x	x	2.46	1.87
<i>nclt_6</i>	50.42	2.97	x	2.14	2.00
<i>nclt_7</i>	x	x	x	4.25	1.66
<i>nclt_8</i>	x	1.78	x	0.90	0.91
<i>nclt_9</i>	50.71	x	x	5.76	5.37
<i>utbm_1</i>	67.16	-	x	15.13	10.00
<i>utbm_2</i>	38.17	-	337.92	21.21	17.33
<i>utbm_3</i>	10.70	-	7.55	10.81	9.83
<i>utbm_4</i>	70.98	-	120.77	15.20	9.06
<i>utbm_5</i>	86.80	-	218.02	13.16	8.25
<i>utbm_6</i>	84.77	-	x	14.67	10.70
<i>utbm_7</i>	62.57	-	565.14	13.24	10.83
<i>ulhk_1</i>	x	1.68	1.55	1.20	1.05
<i>ulhk_2</i>	-	-	-	-	2.88
<i>ulhk_3</i>	x	-	-	-	1.19
<i>ulhk_4</i>	3.11	3.13	3.17	3.24	3.14
<i>ulhk_5</i>	-	-	-	-	2.53

A. Comparison of the State-of-the-Arts

We compare our SR-LIO with four state-of-the-art LIO systems, i.e., LiLi-OM [11], LIO-SAM [14], LINs [13] and Fast-LIO2 [16]. LiLi-OM selects key-sweeps from raw input sweeps, and jointly uses the constraints from LiDAR and IMU in a BA optimization-based framework. LIO-SAM joints the IMU factor and the LiDAR point-to-plane factor into a graph optimization based framework. Both LINs and Fast-LIO2 are iEKF framework based LIO systems, where Fast-LIO2 proposes a more efficient Kalman gain calculation method and a better kd-tree structure based on LINs. For a fair comparison, we obtain the results of the above systems based on the source code provided by the authors.

Results in Table III demonstrate that our SR-LIO outper-

TABLE IV
SWEEP FREQUENCY COMPARISON OF STATE-OF-THE-ARTS

	LiLi-OM [11]	LIO-SAM [14]	LINs [13]	Fast-LIO2 [16]	Ours
<i>nclt</i>	7	7	7	7	20
<i>utbm</i>	10	10	10	10	30
<i>ulhk</i>	10	10	10	10	30

forms state-of-the-arts for almost all sequences in terms of smaller ATE. Although our accuracy is not the best on *nclt_8* and *ulhk_4*, we are very close to the best accuracy, where the ATE is only 1cm more on *nclt_8* and 3cm more on *ulhk_4*. “-” means the corresponding value is not available. LIO-SAM needs 9-axis IMU data as input, while the *utbm* dataset only provides 6-axis IMU data. Therefore, we cannot provide the results of LIO-SAM on the *utbm* dataset. In addition, the frequency of the ground-truth pose of the *ulhk* dataset is too low (i.e., 1 Hz), which prevents the 10 Hz poses estimated by state-of-the-arts from being matched to the time stamp of ground-truth poses on some sequences. As a result, we are unable to provide quantitative evaluation for these cases. “x” means the system fails to run entirety on the corresponding sequence. Except for our system and Fast-LIO, other systems break down on several sequences, which also demonstrate the robustness of our system.

Results in Table IV demonstrate that our sweep reconstruction method can provide higher-frequency sweep than existing state-of-the-arts. Limited by the frequency of LiDAR scan (e.g., 10 Hz), the frequency of LIO joint optimization can only be performed at a maximum frequency of 10 Hz. Even if the power of computing resources (e.g., CPU) is assumed to be infinite, LIO-optimization cannot be performed at higher than 10 Hz. However, with the assistance of our sweep reconstruction, the frequency of LiDAR sweep can be increased to an arbitrary value theoretically. In this work, we increase the frequency of LiDAR sweep from 10 Hz to 30 Hz, because 30 Hz is close to the processing frequency of BA based visual [26]–[30] and visual-inertial odometry/SLAM systems [18], [20], [21], [31]. It is worth mentioning that LIO joint optimization is hard to perform at 30 Hz at this stage. However, our sweep reconstruction method breaks through the theoretical limit of 10 Hz, and enables LIO-optimization to have the potential to perform at a higher frequency. As the performance of computing resource (e.g., CPU) improves, performing LIO-optimization at 30 Hz could also be achieved.

B. Ablation Study of Sweep Reconstruction

We examine the impact of sweep reconstruction on pose estimation accuracy by comparing the ATE result with vs. without sweep reconstruction. Without using the proposed sweep reconstruction, the system takes 10 Hz raw input and 10 Hz IMU pre-integration to perform LIO-optimization. In addition, all other configuration parameters are unchanged.

Results in Table V demonstrate that our sweep reconstruction can significantly improve the accuracy and robustness of BA based LIO-optimization, which demonstrate that reducing

TABLE V
ABLATION STUDY OF SWEEP RECONSTRUCTION ON ACCURACY

	Ours w/o Sweep Reconsruction	Ours
<i>nclt_1</i>	229.32	1.55
<i>nclt_2</i>	x	1.53
<i>nclt_3</i>	x	1.57
<i>nclt_4</i>	1.21	1.22
<i>nclt_5</i>	x	1.87
<i>nclt_6</i>	1.84	2.00
<i>nclt_7</i>	15.76	1.66
<i>nclt_8</i>	0.91	0.91
<i>nclt_9</i>	5.63	5.37
<i>utbm_1</i>	40.01	10.00
<i>utbm_2</i>	x	17.33
<i>utbm_3</i>	x	9.83
<i>utbm_4</i>	88.94	9.06
<i>utbm_5</i>	x	8.25
<i>utbm_6</i>	9.90	10.70
<i>utbm_7</i>	x	10.83
<i>ulhk_1</i>	1.10	1.05
<i>ulhk_2</i>	-	2.88
<i>ulhk_3</i>	-	1.19
<i>ulhk_4</i>	3.18	3.14
<i>ulhk_5</i>	-	2.53

TABLE VI
ABLATION STUDY OF MULTI-SEGMENT LIO OPTIMIZATION ON VARIANCE OF VELOCITY IN Z-DIRECTION COMPONENT (UNIT: $0.01m^2/s^2$)

	Multi-Segment LIO Optimization	Non-Multi-Segment LIO Optimization
<i>nclt_1</i>	9.6	x
<i>nclt_2</i>	3.4	6.7
<i>nclt_3</i>	4.2	6.2
<i>nclt_4</i>	3.7	6.7
<i>nclt_5</i>	4.8	10.1
<i>nclt_6</i>	4.7	9.8
<i>nclt_7</i>	4.0	x
<i>nclt_8</i>	2.7	5.9
<i>nclt_9</i>	4.2	8.3

the IMU pre-integration error is very importance for the success of a BA based LIO framework.

C. Ablation Study of Multi-Segment LIO Optimization

As presented in Sec. V-F1, the proposed multi-segment LIO optimization aims to make the states during $[t_{b_{i+1}}, t_{e_{i+1}}]$ can be optimized equally. To examine the importance of multi-segment LIO optimization, we compare our solution with an alternative method without using IMU pre-integration residuals as constraints for all states during $[t_{b_{i+1}}, t_{e_{i+1}}]$ (e.g., named “non-multi-segment LIO optimization”). As illustrated in Fig. 5, only the variables at time stamp $t_{b_{i+1}}$, t_{e_i} and $t_{e_{i+1}}$ are optimized during non-multi-segment LIO optimization. Without constraining the state at $t_{b_{i+1}}$ using the IMU pre-integration residuals, the velocity, accelerometer bias, gyroscope bias (i.e., $\mathbf{v}_{b_{i+1}}^w$, $\mathbf{b}_{a_{b_{i+1}}}^w$, $\mathbf{b}_{\omega_{b_{i+1}}}^w$) cannot be optimized, but only $\mathbf{q}_{b_{i+1}}^w$ and $\mathbf{t}_{b_{i+1}}^w$ can be updated during non-multi-segment LIO optimization. Therefore, after the non-multi-segment optimization, the kinematic relationship between each variable at $t_{b_{i+1}}$ would be inconsistent. This inconsistency does not result in a serious degradation in pose accuracy (i.e., $\mathbf{q}_{b_{i+1}}^w$ and $\mathbf{t}_{b_{i+1}}^w$) as long as the surrounding geometric information

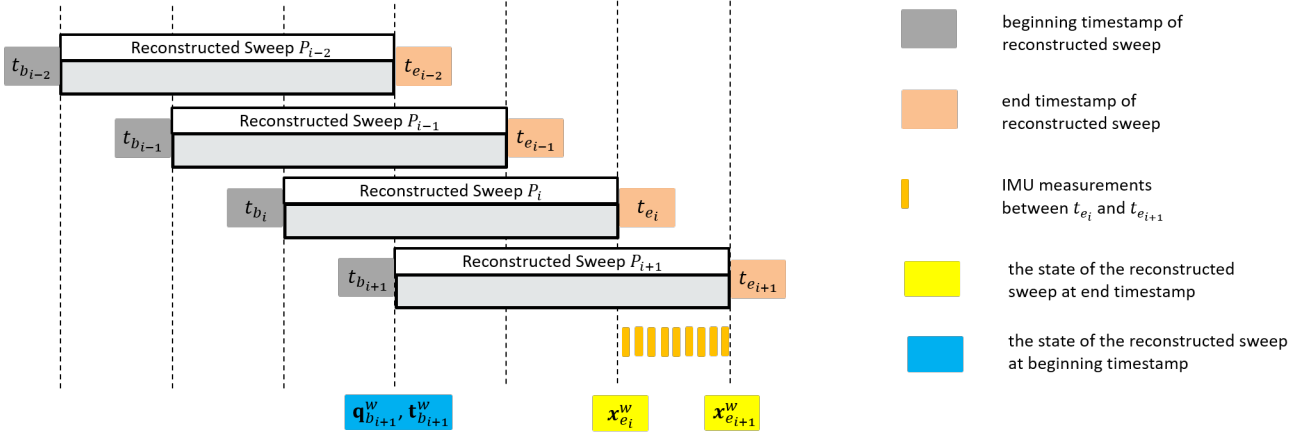


Fig. 5. Illustration of non-multi-segment LIO-optimization, where the variables to be optimized are $\mathbf{q}_{b_{i+1}}^w$, $\mathbf{t}_{b_{i+1}}^w$, $\mathbf{x}_{e_i}^w$ and $\mathbf{x}_{e_{i+1}}^w$. The rotation $\mathbf{q}_{b_{i+1}}^w$ and translation $\mathbf{t}_{b_{i+1}}^w$ at $t_{b_{i+1}}$ can be updated during optimization, but the velocity $\mathbf{v}_{b_{i+1}}^w$, accelerometer bias $\mathbf{b}_{a_{b_{i+1}}}$ and gyroscope bias $\mathbf{b}_{\omega_{b_{i+1}}}$ cannot be updated due to lacking of IMU pre-integration residuals that can constrain them. Therefore, after the non-multi-segment optimization, the kinematic relationship between each variable at $t_{b_{i+1}}$ would be inconsistent.

can also provide strong geometric constraints for ICP point-to-plane residuals. $\mathbf{b}_{a_{b_{i+1}}}^w$ and $\mathbf{b}_{\omega_{b_{i+1}}}^w$ are close to a constant, so it does not matter if they are not updated. However, the accuracy of velocity $\mathbf{v}_{b_{i+1}}^w$ would decrease obviously because it does not change with the updates of $\mathbf{q}_{b_{i+1}}^w$ and $\mathbf{t}_{b_{i+1}}^w$. To verify such negative effect from state inconsistency, we exam the velocity in the Z -direction of all sequences in *nclt*. According to our observation, on the *nclt* dataset, the translation of the vehicle platform in Z -direction component is very small. Therefore, the velocity in the Z -direction should be close to the zero graduation line. A large amplitude of velocity fluctuation in the Z -direction (i.e., a large variance) indicates frequent and large inconsistency between the velocity values and the corresponding poses. Based on the above analysis, we test the variance of velocity in the Z -direction with multi-segment LIO optimization vs. non-multi-segment LIO optimization on all sequences of the *nclt* dataset. Results in Table VI demonstrate that the variance of non-multi-segment LIO optimization is generally higher than multi-segment LIO optimization. That means the velocity estimated by multi-segment LIO optimization is closer to the theoretical zero distribution. On sequences *nclt_1* and *nclt_7*, the state inconsistency can even causes the system to crash.

D. Time Consumption

In this section, we evaluate the runtime breakdown (unit: ms) of our system for all sequences. In general, the most important factors affecting the time cost are the number of ICP point cloud registration, and the number of iteration solutions for each registration. Therefore, for each sequence, we test the time consumption with different number of ICP point cloud registration and different number of iteration solutions for each registration. For each test, we also record the pose accuracy (i.e., ATE) to explore how many registration and iterations are needed to reach the best pose accuracy.

Results in Table VII demonstrate that the accuracy of estimated pose saturates at the 5-5 registration-iteration con-

figuration on all sequences of the *utbm* and *ulhk* datasets, where the average time cost/per sweep is 82.2ms. BA based LIO-optimization (e.g., 69.5ms) takes the most time consumption and map update (e.g., 7.1ms) takes the second time consumption. For *nclt_2*, *nclt_4* and *nclt_8*, the estimated poses also can reach saturation at the 5-5 registration-iteration configuration, where the average time consumption/per sweep is 85.3ms. For *nclt_3*, *nclt_6* and *nclt_7*, the estimated pose can reach saturation at the 10-5 registration-iteration configuration, where the average time consumption/per sweep is 124.7ms. For *nclt_1*, *nclt_5* and *nclt_9*, the estimated pose saturates at the 15-5 registration-iteration configuration, where the average time consumption/per sweep is 150.1ms.

E. Visualization of trajectory and map

In addition to the above quantitative and qualitative evaluations, we also show some visualizations of trajectory and point cloud maps estimated by our SR-LIO. The comparison results between our estimated trajectory and groundtruth on the exemplar sequence *nclt_8* are shown in Fig. 6 (a), where our estimated trajectory and groundtruth almost exactly coincide. Fig. 6 (b)-(d) presents sufficient accuracy of some local structure, where the density of the point clouds is also uniform. More visualization results are also provided in the demo video of our supplementary material which demonstrates the real-time performance of our system for pose estimation and mapping.

VII. CONCLUSION

This paper proposes a novel sweep reconstruction method, which segments and reconstructs raw input sweeps from spinning LiDAR to obtain reconstructed sweeps with higher frequency. This method can not only increase the frequency of LiDAR sweep, but also reduce the error of IMU pre-integration by shortening the integration time interval between two consecutive sweeps. We integrate the proposed sweep reconstruction method into SR-LIO, which is a self-designed

TABLE VII
TIME CONSUMPTION

Seq	Regist -Iter	Time Consumption/Per Sweep (ms)				ATE	Seq	Regist -Iter	Time Consumption/Per Sweep (ms)				ATE
		SR	LIO-Opt	Map Update	Total				SR	LIO-Opt	Map Update	Total	
<i>nclt_1</i>	5-5	x	x	x	x	x	<i>utbm_3</i>	5-5	3	76	9	89	10.40
	10-5	2	115	13	131	2.10		10-5	2	125	9	137	8.96
	15-5	2	132	12	147	1.55		15-5	2	125	9	139	9.83
<i>nclt_2</i>	5-5	2	72	14	89	1.49	<i>utbm_4</i>	5-5	3	78	12	93	9.20
	10-5	2	114	15	132	1.52		10-5	3	127	12	141	9.34
	15-5	2	138	15	155	1.53		15-5	3	127	12	141	9.06
<i>nclt_3</i>	5-5	x	x	x	x	x	<i>utbm_5</i>	5-5	3	79	11	93	8.78
	10-5	3	113	11	127	1.62		10-5	3	124	11	138	8.88
	15-5	2	131	11	144	1.57		15-5	3	123	11	137	8.25
<i>nclt_4</i>	5-5	2	76	7	86	1.25	<i>utbm_6</i>	5-5	2	46	11	60	11.20
	10-5	3	115	7	125	1.23		10-5	2	124	11	138	10.89
	15-5	2	145	7	154	1.22		15-5	2	122	12	136	10.70
<i>nclt_5</i>	5-5	x	x	x	x	x	<i>utbm_7</i>	5-5	3	69	11	83	11.16
	10-5	x	x	x	x	x		10-5	2	128	12	142	10.94
	15-5	2	142	12	156	1.87		15-5	2	128	12	142	10.83
<i>nclt_6</i>	5-5	1	51	9	62	4.72	<i>ulhk_1</i>	5-5	9	70	1	80	1.04
	10-5	3	111	9	123	2.00		10-5	6	100	1	108	1.05
	15-5	2	140	9	152	2.00		15-5	5	116	1	123	1.05
<i>nclt_7</i>	5-5	x	x	x	x	x	<i>ulhk_2</i>	5-5	9	71	1	81	2.88
	10-5	2	111	10	124	1.75		10-5	5	105	1	112	2.88
	15-5	2	131	10	143	1.66		15-5	5	119	1	126	2.88
<i>nclt_8</i>	5-5	3	74	2	81	0.91	<i>ulhk_3</i>	5-5	7	61	2	71	1.20
	10-5	3	111	2	116	0.92		10-5	5	97	2	104	1.19
	15-5	2	133	2	138	0.91		15-5	5	119	2	126	1.19
<i>nclt_9</i>	5-5	x	x	x	x	x	<i>ulhk_4</i>	5-5	8	66	2	77	3.14
	10-5	x	x	x	x	x		10-5	6	94	2	103	3.14
	15-5	3	133	14	149	5.37		15-5	6	111	2	119	3.14
<i>utbm_1</i>	5-5	3	76	11	91	10.29	<i>ulhk_5</i>	5-5	8	65	2	76	2.52
	10-5	3	122	11	135	10.01		10-5	6	93	2	102	2.52
	15-5	3	123	11	137	10.00		15-5	6	107	2	115	2.53
<i>utbm_2</i>	5-5	3	77	12	92	18.17							
	10-5	2	124	12	139	16.84							
	15-5	2	125	12	139	17.33							

BA based LIO system. SR-LIO first down-samples the 10Hz input sweep, and then performs sweep reconstruction to obtain the 30Hz reconstructed sweeps. Next, we perform multi-segment joint optimization for each reconstructed sweep. After the states of the segments of a current reconstructed sweep are optimized, we update the map without adding the same point cloud repeatedly.

The proposed SR-LIO achieves the state-of-the-art accuracy on three public datasets. Meanwhile, the proposed sweep reconstruction method demonstrates its potential to improve the frequency of LIO-optimization.

APPENDIX

I. THE FORMULA OF IMU PRE-INTEGRATION

In this section, we describe the detailed formula and the error state kinematics for the pre-integration of all IMU measurements. We denote α , β , γ as the pre-integration of translation, velocity, rotation respectively from IMU measurements. Accordingly, the calculated pre-integrations between P_i and P_{i+1} in the corresponding IMU coordinates o_{e_i} and $o_{e_{i+1}}$ are denoted as $\hat{\alpha}_{e_{i+1}}^{e_i}$, $\hat{\beta}_{e_{i+1}}^{e_i}$, $\hat{\gamma}_{e_{i+1}}^{e_i}$, which are obtained as:

$$\begin{aligned}
 \hat{\alpha}_{n+1}^{e_i} &= \hat{\alpha}_n^{e_i} + \hat{\beta}_n^{e_i} \delta t + \frac{1}{2} \mathbf{R}(\hat{\gamma}_n^{e_i}) (\hat{\mathbf{a}}_n - \mathbf{b}_{\mathbf{a}_{e_i}}) \delta t^2 \\
 \hat{\beta}_{n+1}^{e_i} &= \hat{\beta}_n^{e_i} + \mathbf{R}(\hat{\gamma}_n^{e_i}) (\hat{\mathbf{a}}_n - \mathbf{b}_{\mathbf{a}_{e_i}}) \delta t \\
 \hat{\gamma}_{n+1}^{e_i} &= \hat{\gamma}_n^{e_i} \otimes \begin{bmatrix} 1 \\ \frac{1}{2} (\hat{\boldsymbol{\omega}}_n - \mathbf{b}_{\boldsymbol{\omega}_{e_i}}) \delta t \end{bmatrix}
 \end{aligned} \quad (24)$$

where e_i is the end time stamp of P_i , n and $n+1$ are two time instants of obtaining an IMU measurement during $[t_{e_i}, t_{e_{i+1}}]$, δt is the time interval between n and $n+1$. We iteratively increase n from 0 to $(t_{e_{i+1}} - t_{e_i}) / \delta t$ to obtain $\hat{\alpha}_{e_{i+1}}^{e_i}$, $\hat{\beta}_{e_{i+1}}^{e_i}$ and $\hat{\gamma}_{e_{i+1}}^{e_i}$, where (\cdot) denotes the approximated value of real data $\alpha_{e_{i+1}}^{e_i}$, $\beta_{e_{i+1}}^{e_i}$ and $\gamma_{e_{i+1}}^{e_i}$ which contains errors arising from the ignorance of the measurement noises and inaccurate bias.

As shown in Eq. 25, we follow [20] to derive the error state kinematics in discrete time to propagate the covariance matrix with the second-order terms of δt being omitted.

$$\begin{bmatrix} \delta \hat{\alpha}_{n+1}^{e_i} \\ \delta \hat{\beta}_{n+1}^{e_i} \\ \delta \hat{\boldsymbol{\theta}}_{n+1}^{e_i} \\ \delta \mathbf{b}_{\mathbf{a}_{n+1}} \\ \delta \mathbf{b}_{\boldsymbol{\omega}_{n+1}} \end{bmatrix} = \begin{bmatrix} \mathbf{0} & \mathbf{0} & \mathbf{0} & \mathbf{0} \\ -\mathbf{R}_n^{e_i} \delta t & \mathbf{0} & \mathbf{0} & \mathbf{0} \\ \mathbf{0} & -\mathbf{I} \delta t & \mathbf{0} & \mathbf{0} \\ \mathbf{0} & \mathbf{0} & \mathbf{I} \delta t & \mathbf{0} \\ \mathbf{0} & \mathbf{0} & \mathbf{0} & \mathbf{I} \delta t \end{bmatrix} \begin{bmatrix} \mathbf{n}_{\mathbf{a}} \\ \mathbf{n}_{\boldsymbol{\omega}} \\ \mathbf{n}_{\mathbf{b}_{\mathbf{a}}} \\ \mathbf{n}_{\mathbf{b}_{\boldsymbol{\omega}}} \end{bmatrix} + \begin{bmatrix} \mathbf{I} & \mathbf{I} \delta t & \mathbf{0} & \mathbf{0} & \mathbf{0} \\ \mathbf{0} & \mathbf{I} & -\mathbf{R}_n^{e_i} [\hat{\mathbf{a}}_n - \mathbf{b}_{\mathbf{a}_n}]_{\times} \delta t & -\mathbf{R}_n^{e_i} \delta t & \mathbf{0} \\ \mathbf{0} & \mathbf{0} & \mathbf{I} - [\hat{\boldsymbol{\omega}}_n - \mathbf{b}_{\boldsymbol{\omega}_n}]_{\times} \delta t & \mathbf{0} & -\mathbf{I} \delta t \\ \mathbf{0} & \mathbf{0} & \mathbf{0} & \mathbf{I} & \mathbf{0} \\ \mathbf{0} & \mathbf{0} & \mathbf{0} & \mathbf{0} & \mathbf{I} \end{bmatrix} \begin{bmatrix} \delta \hat{\alpha}_n^{e_i} \\ \delta \hat{\beta}_n^{e_i} \\ \delta \hat{\boldsymbol{\theta}}_n^{e_i} \\ \delta \mathbf{b}_{\mathbf{a}_n} \\ \delta \mathbf{b}_{\boldsymbol{\omega}_n} \end{bmatrix} \quad (25)$$

where $[\cdot]_{\times}$ indicates the skew symmetric matrix corresponding to a vector, $\mathbf{R}_n^{e_i}$ means $\mathbf{R}(\hat{\gamma}_n^{e_i})$, and $\delta \hat{\boldsymbol{\theta}}_n^{e_i}$ is the perturbation of rotation that is used to define the error term of $\hat{\gamma}_n^{e_i}$, which is

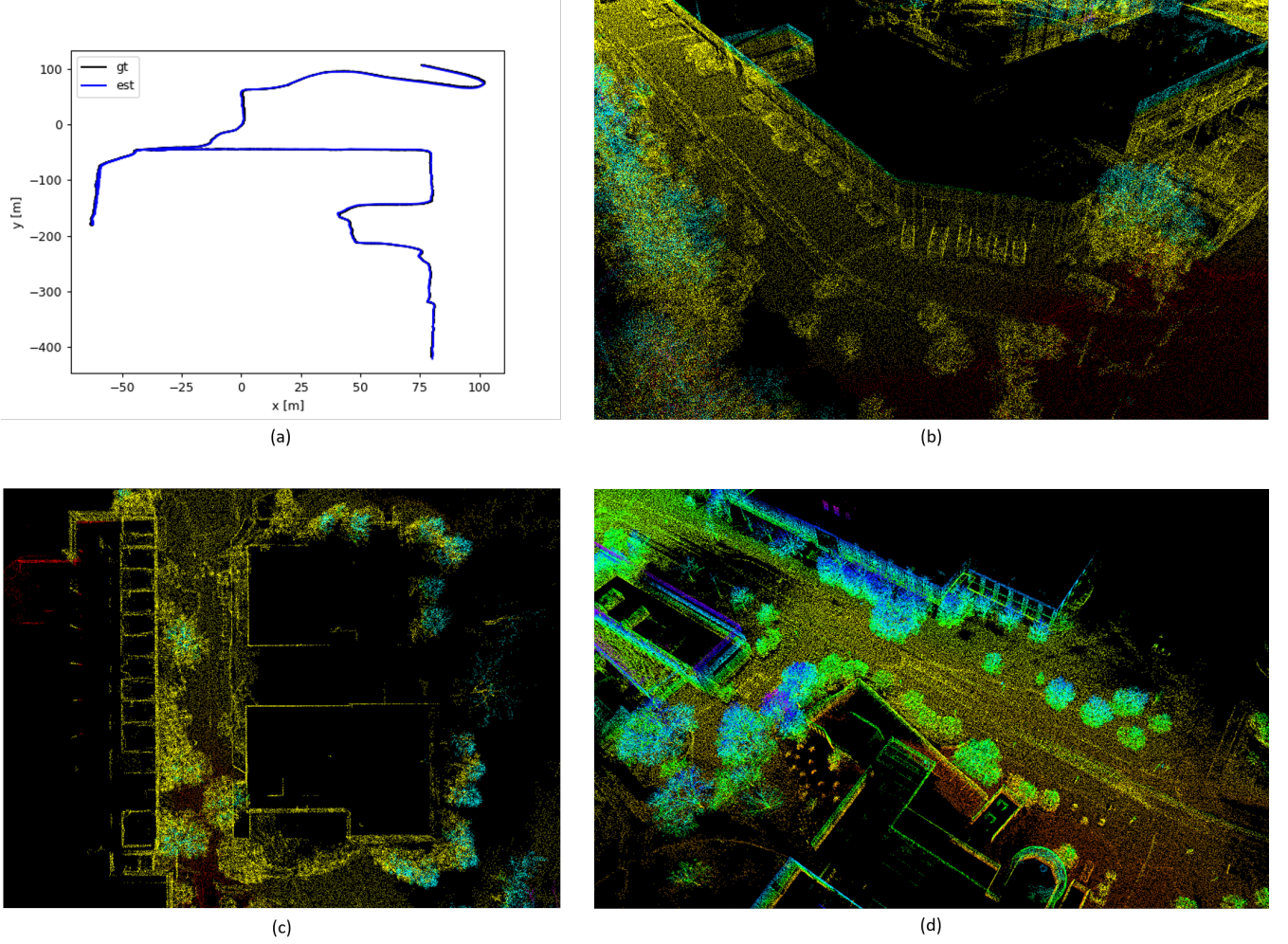


Fig. 6. (a) The comparison results between our estimated trajectory and groundtruth on the exemplar sequence *nclt_8*. (b)–(d) are three local point cloud map.

written as $\gamma_n^{e_i} \approx \hat{\gamma}_n^{e_i} \otimes \begin{bmatrix} 1 \\ \frac{1}{2}\delta\theta_n^{e_i} \end{bmatrix}$. \mathbf{n}_a , \mathbf{n}_ω , \mathbf{n}_{b_a} and \mathbf{n}_{b_ω} have been defined in Sec. V-C1. Eq. 25 can then be summarized as:

$$\delta\mathbf{z}_{n+1}^{e_i} = \mathbf{F}_n \delta\mathbf{z}_n^{e_i} + \mathbf{G}_n \mathbf{n} \quad (26)$$

According to forward propagation of covariance [20], the covariance matrix $\mathbf{P}_{n+1}^{e_i}$ can be computed recursively by the first-order discrete-time covariance updated with the initial covariance $\mathbf{P}_{e_i}^{e_i} = \mathbf{0}$:

$$\mathbf{P}_{n+1}^{e_i} = \mathbf{F}_n \mathbf{P}_n^{e_i} \mathbf{F}_n^T + \mathbf{G}_n \mathbf{Q} \mathbf{G}_n^T \quad (27)$$

where \mathbf{Q} is the diagonal covariance matrix of noise (σ_a^2 , σ_ω^2 , $\sigma_{b_a}^2$, $\sigma_{b_\omega}^2$).

Meanwhile, the first-order Jacobian matrix $\mathbf{J}_{e_{i+1}}^{e_i}$ of $\delta\mathbf{z}_{e_{i+1}}^{e_i}$ with respect to $\delta\mathbf{z}_{e_i}^{e_i}$ can be also computed with the initial $\mathbf{J}_{e_i}^{e_i} = \mathbf{I}$:

$$\mathbf{J}_{n+1}^{e_i} = \mathbf{F}_n \mathbf{J}_n^{e_i} \quad (28)$$

Using this recursive formulation, we get the covariance matrix $\mathbf{P}_{e_{i+1}}^{e_i}$ that is utilized for weighting the IMU residuals in LIO-optimization, and $\mathbf{J}_{e_{i+1}}^{e_i}$ that is as the derivative of the IMU

pre-integration (i.e., $\alpha_{e_{i+1}}^{e_i}$, $\beta_{e_{i+1}}^{e_i}$ and $\gamma_{e_{i+1}}^{e_i}$) with respect to biases can be written as:

$$\begin{aligned} \alpha_{e_{i+1}}^{e_i} &\approx \hat{\alpha}_{e_{i+1}}^{e_i} + \mathbf{J}_{b_a}^\alpha \delta\mathbf{b}_{a_{e_i}} + \mathbf{J}_{b_\omega}^\alpha \delta\mathbf{b}_{\omega_{e_i}} \\ \beta_{e_{i+1}}^{e_i} &\approx \hat{\beta}_{e_{i+1}}^{e_i} + \mathbf{J}_{b_a}^\beta \delta\mathbf{b}_{a_{e_i}} + \mathbf{J}_{b_\omega}^\beta \delta\mathbf{b}_{\omega_{e_i}} \\ \gamma_{e_{i+1}}^{e_i} &\approx \hat{\gamma}_{e_{i+1}}^{e_i} \otimes \begin{bmatrix} 1 \\ \frac{1}{2}\mathbf{J}_\omega^\gamma \delta\mathbf{b}_{\omega_{e_i}} \end{bmatrix} \end{aligned} \quad (29)$$

where $\mathbf{J}_{b_a}^\alpha$, $\mathbf{J}_{b_\omega}^\alpha$, $\mathbf{J}_{b_a}^\beta$, $\mathbf{J}_{b_\omega}^\beta$ and \mathbf{J}_ω^γ are the sub-block matrices in $\mathbf{J}_{e_{i+1}}^{e_i}$ whose locations are corresponding to $\frac{\partial \alpha_{e_{i+1}}^{e_i}}{\partial \mathbf{b}_{a_{e_i}}}$, $\frac{\partial \alpha_{e_{i+1}}^{e_i}}{\partial \mathbf{b}_{\omega_{e_i}}}$, $\frac{\partial \beta_{e_{i+1}}^{e_i}}{\partial \mathbf{b}_{a_{e_i}}}$, $\frac{\partial \beta_{e_{i+1}}^{e_i}}{\partial \mathbf{b}_{\omega_{e_i}}}$ and $\frac{\partial \gamma_{e_{i+1}}^{e_i}}{\partial \mathbf{b}_{\omega_{e_i}}}$ respectively.

APPENDIX

II. THE JACOBIAN OF POINT-TO-PLANE RESIDUAL

In this section, we detail the Jacobian of the adopted point-to-plane residual in this work. For instance, in Eq. 17, the residual is r^P and the variables are $\mathbf{t}_{b_{i+1}}^w$, $\mathbf{t}_{e_{i-1}}^w$, $\mathbf{q}_{b_{i+1}}^w$, $\mathbf{q}_{e_{i-1}}^w$. Since the degree of freedom (DOF) of quaternion (e.g., $\mathbf{q}_{b_{i+1}}^w$, $\mathbf{q}_{e_{i-1}}^w$) is 3, when taking derivatives and update variables, we usually express it in the form of angle axis (e.g., $\theta_{b_{i+1}}^w$, $\theta_{e_{i-1}}^w$),

where the dimensionality of DOF (i.e., 3) is the same as the number of variables (i.e., 3) for angle axis. Then the Jacobian is expressed as:

$$\mathbf{J}_p = \begin{bmatrix} \frac{\partial r^p}{\partial \mathbf{t}_{b_{i+1}}^w} & \frac{\partial r^p}{\partial \mathbf{t}_{e_{i-1}}^w} & \frac{\partial r^p}{\partial \mathbf{q}_{b_{i+1}}^w} & \frac{\partial r^p}{\partial \mathbf{q}_{e_{i-1}}^w} \end{bmatrix} \quad (30)$$

where

$$\begin{aligned} \frac{\partial r^p}{\partial \mathbf{t}_{b_{i+1}}^w} &= \mathbf{n}^T \omega_p (1 - \alpha) \\ \frac{\partial r^p}{\partial \mathbf{t}_{e_{i-1}}^w} &= \mathbf{n}^T \omega_p \alpha \\ \frac{\partial r^p}{\partial \mathbf{q}_{b_{i+1}}^w} &\approx -\mathbf{n}^T \mathbf{R}_{b_{i+1}}^w [\mathbf{p}]_{\times} \omega_p (1 - \alpha) \\ \frac{\partial r^p}{\partial \mathbf{q}_{e_{i-1}}^w} &\approx -\mathbf{n}^T \mathbf{R}_{e_{i-1}}^w [\mathbf{p}]_{\times} \omega_p \alpha \end{aligned} \quad (31)$$

where $[\cdot]_x$ indicates the skew symmetric matrix corresponding to a vector, the definition of α , \mathbf{n}^T and ω_p are the same as Eq. 17.

APPENDIX

III. THE JACOBIAN OF IMU PRE-INTEGRATION RESIDUAL

In this section, we detail the Jacobian of the IMU pre-integration residual introduced in Eq. 19 and 20 and 21. For instance, in Eq. 19, the residual is $\mathbf{r}_{oe_{i+1}}^{e_i}$ and the variables are $\mathbf{t}_{e_i}^w$, $\mathbf{t}_{e_{i+1}}^w$, $\mathbf{q}_{e_i}^w$, $\mathbf{q}_{e_{i+1}}^w$, $\mathbf{v}_{e_i}^w$, $\mathbf{v}_{e_{i+1}}^w$, $\mathbf{b}_{a_{e_i}}$, $\mathbf{b}_{a_{e_{i+1}}}$, $\mathbf{b}_{\omega_{e_i}}$ and $\mathbf{b}_{\omega_{e_{i+1}}}$. Same as Appendix-II, we express $\mathbf{q}_{e_i}^w$ and $\mathbf{q}_{e_{i+1}}^w$ as $\theta_{e_i}^w$ and $\theta_{e_{i+1}}^w$. Then the Jacobian is expressed as:

$$\mathbf{J}_o^{e_i} = \begin{bmatrix} \frac{\partial \mathbf{r}_{t_{e_{i+1}}}^{e_i}}{\partial \mathbf{t}_{e_i}^w} & \frac{\partial \mathbf{r}_{t_{e_{i+1}}}^{e_i}}{\partial \theta_{e_i}^w} & \frac{\partial \mathbf{r}_{t_{e_{i+1}}}^{e_i}}{\partial \mathbf{v}_{e_i}^w} & \frac{\partial \mathbf{r}_{t_{e_{i+1}}}^{e_i}}{\partial \mathbf{b}_{a_{e_i}}} & \frac{\partial \mathbf{r}_{t_{e_{i+1}}}^{e_i}}{\partial \mathbf{b}_{\omega_{e_i}}} \\ 0 & \frac{\partial \mathbf{r}_{q_{e_{i+1}}}^{e_i}}{\partial \theta_{e_i}^w} & 0 & 0 & \frac{\partial \mathbf{r}_{q_{e_{i+1}}}^{e_i}}{\partial \mathbf{b}_{\omega_{e_i}}} \\ 0 & \frac{\partial \mathbf{r}_{v_{e_{i+1}}}^{e_i}}{\partial \theta_{e_i}^w} & \frac{\partial \mathbf{r}_{v_{e_{i+1}}}^{e_i}}{\partial \mathbf{v}_{e_i}^w} & \frac{\partial \mathbf{r}_{v_{e_{i+1}}}^{e_i}}{\partial \mathbf{b}_{a_{e_i}}} & \frac{\partial \mathbf{r}_{v_{e_{i+1}}}^{e_i}}{\partial \mathbf{b}_{\omega_{e_i}}} \\ 0 & 0 & 0 & -\mathbf{I} & 0 \\ 0 & 0 & 0 & 0 & \mathbf{I} \end{bmatrix} \quad (32)$$

$$\mathbf{J}_o^{e_{i+1}} = \begin{bmatrix} \frac{\partial \mathbf{r}_{t_{e_{i+1}}}^{e_{i+1}}}{\partial \mathbf{t}_{e_{i+1}}^w} & 0 & 0 & 0 & 0 \\ 0 & \frac{\partial \mathbf{r}_{q_{e_{i+1}}}^{e_{i+1}}}{\partial \theta_{e_{i+1}}^w} & 0 & 0 & 0 \\ 0 & 0 & \frac{\partial \mathbf{r}_{v_{e_{i+1}}}^{e_{i+1}}}{\partial \mathbf{v}_{e_{i+1}}^w} & 0 & 0 \\ 0 & 0 & 0 & \mathbf{I} & 0 \\ 0 & 0 & 0 & 0 & \mathbf{I} \end{bmatrix} \quad (33)$$

where

$$\frac{\partial \mathbf{r}_{t_{e_{i+1}}}^{e_i}}{\partial \mathbf{t}_{e_i}^w} = -\mathbf{R}_w^{e_i} \quad (34)$$

$$\frac{\partial \mathbf{r}_{t_{e_{i+1}}}^{e_{i+1}}}{\partial \theta_{e_i}^w} = \left[\mathbf{R}_w^{e_i} \left(\mathbf{t}_{e_{i+1}}^w - \mathbf{t}_{e_i}^w - \mathbf{v}_{e_i}^w \Delta t + \frac{1}{2} \mathbf{g}^w \Delta t^2 \right) \right]^\wedge \quad (35)$$

$$\frac{\partial \mathbf{r}_{t_{e_{i+1}}}^{e_{i+1}}}{\partial \mathbf{v}_{e_i}^w} = -\mathbf{R}_w^{e_i} \Delta t \quad (36)$$

$$\frac{\partial \mathbf{r}_{t_{e_{i+1}}}^{e_{i+1}}}{\partial \mathbf{b}_{a_{e_i}}} = -\mathbf{J}_{b_a}^\alpha \quad (37)$$

$$\frac{\partial \mathbf{r}_{t_{e_{i+1}}}^{e_i}}{\partial \mathbf{b}_{\omega_{e_i}}} = -\mathbf{J}_{b_\omega}^\alpha \quad (38)$$

$$\frac{\partial \mathbf{r}_{q_{e_{i+1}}}^{e_i}}{\partial \theta_{e_i}^w} = -\mathcal{L} \left[\mathbf{q}_{e_{i+1}}^{w-1} \otimes \mathbf{q}_{e_i}^w \right] \mathcal{R} \left[\gamma_{e_{i+1}}^{e_i} \right] \quad (39)$$

$$\frac{\partial \mathbf{r}_{q_{e_{i+1}}}^{e_i}}{\partial \mathbf{b}_{\omega_{e_i}}} = -\mathcal{L} \left[\mathbf{q}_{e_{i+1}}^{w-1} \otimes \mathbf{q}_{e_i}^w \otimes \gamma_{e_{i+1}}^{e_i} \right] \mathbf{J}_{b_\omega}^\gamma \quad (40)$$

$$\frac{\partial \mathbf{r}_{v_{e_{i+1}}}^{e_i}}{\partial \theta_{e_i}^w} = \left[\mathbf{R}_w^{e_i} \left(\mathbf{v}_{e_{i+1}}^w - \mathbf{v}_{e_i}^w + \mathbf{g}^w \Delta t \right) \right]^\wedge \quad (41)$$

$$\frac{\partial \mathbf{r}_{v_{e_{i+1}}}^{e_i}}{\partial \mathbf{v}_{e_i}^w} = -\mathbf{R}_w^{e_i} \quad (42)$$

$$\frac{\partial \mathbf{r}_{v_{e_{i+1}}}^{e_i}}{\partial \mathbf{b}_{a_{e_i}}} = -\mathbf{J}_{b_a}^\beta \quad (43)$$

$$\frac{\partial \mathbf{r}_{v_{e_{i+1}}}^{e_i}}{\partial \mathbf{b}_{\omega_{e_i}}} = -\mathbf{J}_{b_\omega}^\beta \quad (44)$$

$$\frac{\partial \mathbf{r}_{t_{e_{i+1}}}^{e_i}}{\partial \mathbf{t}_{e_{i+1}}^w} = \mathbf{R}_w^{e_i} \quad (45)$$

$$\frac{\partial \mathbf{r}_{q_{e_{i+1}}}^{e_i}}{\partial \theta_{e_{i+1}}^w} = \mathcal{L} \left[\gamma_{e_{i+1}}^{e_i-1} \otimes \mathbf{q}_{e_i}^{w-1} \otimes \mathbf{q}_{e_{i+1}}^w \right] \quad (46)$$

$$\frac{\partial \mathbf{r}_{v_{e_{i+1}}}^{e_i}}{\partial \mathbf{v}_{e_{i+1}}^w} = \mathbf{R}_w^{e_i} \quad (47)$$

$\mathcal{L}[\cdot]$ is the left multiplication matrix of quaternion, and $\mathcal{R}[\cdot]$ is the right multiplication matrix of quaternion. $[\cdot]^\wedge$ indicates the vector corresponding to a skew symmetric matrix.

APPENDIX

IV. THE JACOBIAN OF IMU PRE-INTEGRATION RESIDUAL

In this section, we detail the Jacobian of the consistency residual introduced in Eq. 22. The residual is \mathbf{r}_c and the variables are $\mathbf{t}_{b_{i+1}}^w$, $\mathbf{q}_{b_{i+1}}^w$, $\mathbf{v}_{b_{i+1}}^w$, $\mathbf{b}_{a_{b_{i+1}}}$, $\mathbf{b}_{\omega_{b_{i+1}}}$. Same as Appendix-II and III, we express $\mathbf{q}_{b_{i+1}}^w$ as $\theta_{b_{i+1}}^w$. Then the Jacobian is expressed as:

$$\mathbf{J}_c = \begin{bmatrix} \frac{\partial \mathbf{r}_c^t}{\partial \mathbf{t}_{b_{i+1}}^w} & 0 & 0 & 0 & 0 \\ 0 & \frac{\partial \mathbf{r}_c^q}{\partial \theta_{b_{i+1}}^w} & 0 & 0 & 0 \\ 0 & 0 & \frac{\partial \mathbf{r}_c^v}{\partial \mathbf{v}_{b_{i+1}}^w} & 0 & 0 \\ 0 & 0 & 0 & \frac{\partial \mathbf{r}_c^{b_a}}{\partial \mathbf{b}_{a_{b_{i+1}}}} & 0 \\ 0 & 0 & 0 & 0 & \frac{\partial \mathbf{r}_c^{b_\omega}}{\partial \mathbf{b}_{\omega_{b_{i+1}}}} \end{bmatrix} \quad (48)$$

where

$$\frac{\partial \mathbf{r}_c^t}{\partial \mathbf{t}_{b_{i+1}}^w} = \frac{\partial \mathbf{r}_c^v}{\partial \mathbf{v}_{b_{i+1}}^w} = \frac{\partial \mathbf{r}_c^{b_a}}{\partial \mathbf{b}_{a_{b_{i+1}}}} = \frac{\partial \mathbf{r}_c^{b_\omega}}{\partial \mathbf{b}_{\omega_{b_{i+1}}}} = \mathbf{I} \quad (49)$$

$$\frac{\partial \mathbf{r}_c^q}{\partial \theta_{b_{i+1}}^w} \approx \left[\frac{\mathbf{r}_c^q}{2} \right]_w \mathbf{I} + \left[\left[\frac{\mathbf{r}_c^q}{2} \right]_{xyz} \right]_{\times} \quad (50)$$

where $[\cdot]_w$ extracts the w part of a quaternion \mathbf{q} for error state representation.

REFERENCES

- [1] J. Zhang and S. Singh, "Loam: Lidar odometry and mapping in real-time," in *Robotics: Science and Systems*, vol. 2, no. 9. Berkeley, CA, 2014, pp. 1–9.
- [2] —, "Low-drift and real-time lidar odometry and mapping," *Autonomous Robots*, vol. 41, no. 2, pp. 401–416, 2017.
- [3] T. Shan and B. Englot, "Lego-loam: Lightweight and ground-optimized lidar odometry and mapping on variable terrain," in *2018 IEEE/RSJ International Conference on Intelligent Robots and Systems (IROS)*. IEEE, 2018, pp. 4758–4765.
- [4] H. Wang, C. Wang, and L. Xie, "Intensity scan context: Coding intensity and geometry relations for loop closure detection," in *2020 IEEE International Conference on Robotics and Automation (ICRA)*. IEEE, 2020, pp. 2095–2101.
- [5] J.-E. Deschaud, "Imls-slam: Scan-to-model matching based on 3d data," in *2018 IEEE International Conference on Robotics and Automation (ICRA)*. IEEE, 2018, pp. 2480–2485.
- [6] P. Dellenbach, J.-E. Deschaud, B. Jacquet, and F. Goulette, "Ct-icp: Real-time elastic lidar odometry with loop closure," in *2022 International Conference on Robotics and Automation (ICRA)*. IEEE, 2022, pp. 5580–5586.
- [7] J. Behley and C. Stachniss, "Efficient surfel-based slam using 3d laser range data in urban environments," in *Robotics: Science and Systems*, vol. 2018, 2018, p. 59.
- [8] G. C. Sharp, S. W. Lee, and D. K. Wehe, "Icp registration using invariant features," *IEEE Transactions on Pattern Analysis and Machine Intelligence*, vol. 24, no. 1, pp. 90–102, 2002.
- [9] K.-L. Low, "Linear least-squares optimization for point-to-plane icp surface registration," *Chapel Hill, University of North Carolina*, vol. 4, no. 10, pp. 1–3, 2004.
- [10] A. Segal, D. Haehnel, and S. Thrun, "Generalized-icp," in *Robotics: science and systems*, vol. 2, no. 4. Seattle, WA, 2009, p. 435.
- [11] K. Li, M. Li, and U. D. Hanebeck, "Towards high-performance solid-state-lidar-inertial odometry and mapping," *IEEE Robotics and Automation Letters*, vol. 6, no. 3, pp. 5167–5174, 2021.
- [12] H. Ye, Y. Chen, and M. Liu, "Tightly coupled 3d lidar inertial odometry and mapping," in *2019 International Conference on Robotics and Automation (ICRA)*. IEEE, 2019, pp. 3144–3150.
- [13] C. Qin, H. Ye, C. E. Pranata, J. Han, S. Zhang, and M. Liu, "Lins: A lidar-inertial state estimator for robust and efficient navigation," in *2020 IEEE international conference on robotics and automation (ICRA)*. IEEE, 2020, pp. 8899–8906.
- [14] T. Shan, B. Englot, D. Meyers, W. Wang, C. Ratti, and D. Rus, "Lio-sam: Tightly-coupled lidar inertial odometry via smoothing and mapping," in *2020 IEEE/RSJ international conference on intelligent robots and systems (IROS)*. IEEE, 2020, pp. 5135–5142.
- [15] W. Xu and F. Zhang, "Fast-lío: A fast, robust lidar-inertial odometry package by tightly-coupled iterated kalman filter," *IEEE Robotics and Automation Letters*, vol. 6, no. 2, pp. 3317–3324, 2021.
- [16] W. Xu, Y. Cai, D. He, J. Lin, and F. Zhang, "Fast-lío2: Fast direct lidar-inertial odometry," *IEEE Transactions on Robotics*, 2022.
- [17] K. Chen, R. Nemiroff, and B. T. Lopez, "Direct lidar-inertial odometry," *arXiv preprint arXiv:2203.03749*, 2022.
- [18] C. Forster, L. Carlone, F. Dellaert, and D. Scaramuzza, "On-manifold preintegration for real-time visual-inertial odometry," *IEEE Transactions on Robotics*, vol. 33, no. 1, pp. 1–21, 2016.
- [19] Y. Cai, W. Xu, and F. Zhang, "ikd-tree: An incremental kd tree for robotic applications," *arXiv preprint arXiv:2102.10808*, 2021.
- [20] T. Qin, P. Li, and S. Shen, "Vins-mono: A robust and versatile monocular visual-inertial state estimator," *IEEE Transactions on Robotics*, vol. 34, no. 4, pp. 1004–1020, 2018.
- [21] C. Campos, R. Elvira, J. J. G. Rodríguez, J. M. Montiel, and J. D. Tardós, "Orb-slam3: An accurate open-source library for visual, visual-inertial, and multimap slam," *IEEE Transactions on Robotics*, vol. 37, no. 6, pp. 1874–1890, 2021.
- [22] P. Geneva, K. Eckenhoff, W. Lee, Y. Yang, and G. Huang, "OpenVins: A research platform for visual-inertial estimation," in *2020 IEEE International Conference on Robotics and Automation (ICRA)*. IEEE, 2020, pp. 4666–4672.
- [23] N. Carlevaris-Bianco, A. K. Ushani, and R. M. Eustice, "University of michigan north campus long-term vision and lidar dataset," *The International Journal of Robotics Research*, vol. 35, no. 9, pp. 1023–1035, 2016.
- [24] Z. Yan, L. Sun, T. Krajník, and Y. Ruichek, "Eu long-term dataset with multiple sensors for autonomous driving," in *2020 IEEE/RSJ International Conference on Intelligent Robots and Systems (IROS)*. IEEE, 2020, pp. 10 697–10 704.
- [25] W. Wen, Y. Zhou, G. Zhang, S. Fahandezh-Saadi, X. Bai, W. Zhan, M. Tomizuka, and L.-T. Hsu, "Urbanloco: A full sensor suite dataset for mapping and localization in urban scenes," in *2020 IEEE International Conference on Robotics and Automation (ICRA)*. IEEE, 2020, pp. 2310–2316.
- [26] R. Mur-Artal, J. M. M. Montiel, and J. D. Tardós, "Orb-slam: a versatile and accurate monocular slam system," *IEEE transactions on robotics*, vol. 31, no. 5, pp. 1147–1163, 2015.
- [27] R. Mur-Artal and J. D. Tardós, "Orb-slam2: An open-source slam system for monocular, stereo, and rgb-d cameras," *IEEE transactions on robotics*, vol. 33, no. 5, pp. 1255–1262, 2017.
- [28] C. Forster, Z. Zhang, M. Gassner, M. Werlberger, and D. Scaramuzza, "Svo: Semidirect visual odometry for monocular and multicamera systems," *IEEE Transactions on Robotics*, vol. 33, no. 2, pp. 249–265, 2016.
- [29] X. Yang, Z. Yuan, D. Zhu, C. Chi, K. Li, and C. Liao, "Robust and efficient rgb-d slam in dynamic environments," *IEEE Transactions on Multimedia*, vol. 23, pp. 4208–4219, 2020.
- [30] Z. Yuan, K. Cheng, J. Tang, and X. Yang, "Rgb-d dso: Direct sparse odometry with rgb-d cameras for indoor scenes," *IEEE Transactions on Multimedia*, 2021.
- [31] Z. Yuan, D. Zhu, C. Chi, J. Tang, C. Liao, and X. Yang, "Visual-inertial state estimation with pre-integration correction for robust mobile augmented reality," in *Proceedings of the 27th ACM International Conference on Multimedia*, 2019, pp. 1410–1418.



Zikang Yuan received the B.E. degree from Huazhong University of Science and Technology (HUST), Wuhan, China, in 2020. He is currently a 3rd year PhD student of HUST, School of Institute of Artificial Intelligence. He has published two papers on ACM MM and two papers on TMM. His research interests include monocular dense mapping, RGB-D simultaneous localization and mapping, visual-inertial state estimation, visual-LiDAR pose estimation and LiDAR-inertial state estimation.



Tianfeng Lang is currently a 4th year B.E. student of HUST, School of Electronic Information and Communications. His research interests include LiDAR-inertial state estimation and LiDAR-inertial-wheel state estimation.



Xin Yang received her PhD degree in University of California, Santa Barbara in 2013. She worked as a Post-doc in Learning-based Multimedia Lab at UCSB (2013-2014). She is current Professor of Huazhong University of Science and Technology School of Electronic Information and Communications. Her research interests include simultaneous localization and mapping, augmented reality, and medical image analysis. She has published over 90 technical papers, including TPAMI, IJCV, TMI, MedIA, CVPR, ECCV, MM, etc., co-authored two books and holds 3 U.S. Patents. Prof. Yang is a member of IEEE and a member of ACM.